Development of Monolithically Integrated Photonic Devices through Simulation and Characterization

by

Roger D'Abreo

A thesis submitted in conformity with the requirements
for the degree of Master of Applied Science
Graduate Department of Electrical and Computer Engineering
University of Toronto

Your file Votre référence
ISBN: 978-0-494-58921-2
Our file Notre référence
ISBN: 978-0-494-58921-2

Abstract

Development of Monolithically Integrated Photonic Devices through Simulation and Characterization

Roger D'Abreo

Master of Applied Science

Graduate Department of Electrical and Computer Engineering

University of Toronto

2009

Simulations were carried out to determine the optical properties of 2 different layer structures which have been used in quantum well intermixed devices. The supported modes, effective refractive indices and optimal device dimensions prior to intermixing were reported. 1.5 μm ridge waveguides with 600 μm bend radii are shown to be suitable for minimizing loss. A first approximation to the intermixed structures were also simulated.

An Asymmetric Mach-Zehnder Interferometer (AMZI) fabricated using a sputtered SiO_2 Quantum Well Intermixing (QWI) process was also characterized. A 100 GHz channel spacing with an extinction ratio up to 16 dB was observed. Tuning of the device was achieved using current injection. A 0.45 nm tuning range was achieved at 15 mA of injected current.

The design of a monolithically integrated all optical binary half-adder is also presented, with physical dimensions based on the results of the previous simulations.

Acknowledgements

The work that was completed in this thesis would not have been possible without the ongoing support of my supervisor, colleagues, friends and family. First and foremost I would like thank my supervisor, Professor Stewart Aitchison. His continued guidance, encouragement and mentorship with respect to my thesis as well as many of the major decisions I have made over the past 2 years is greatly appreciated. I have truly enjoyed working under his supervision.

I am grateful to thank Dr. Aaron Zilke, for the invaluable help and advice he provided me with throughout my thesis. Without his assistance I might never have been able to get results from the AMZI's. His expertise in optics and the hours he spent with me in the lab have been extremely helpful.

I would also like to thank Professor Li Qian for allowing me to use the facilities in her lab as well as for spending the time to teach me how to use her testbed for high speed all optical switches.

To my friends, especially Harnik Shukla and Pier Olivier DeViveiros, I thank them for their unconditional friendship and support over the past 6 years. I couldn't have asked for better friends.

Lastly to my family, for always supporting the decisions I have made and being there for me when I need them the most.

Contents

List of Figures

List of Tables

List of Acronyms

WDM Wavelength Division Multiplexing

mux/demux Multiplexer/Demultiplexer

AMZI Asymmetric Mach-Zehnder Interferometer

SOI Silicon on Insulator

FLC Ferroelectric Liquid Crystal

CMOS Complementary Metal-Oxide Semiconductor

MZ-TOAD Mach-Zehnder Terahertz Optical Asymmetric Demultiplexer

SOA Semiconductor Optical Amplifier

QWI Quantum Well Intermixing

DI Delayed Interferometer

MMI Multimode Interference

ITU International Telecommunication Union

DWDM Dense Wavelength Division Multiplexing

MQW Multiple Quantum Well

MOCVD Metal Organic Chemical Vapour Deposition

GRIN Graded Refractive Index

PECVD Plasma Enhanced Chemical Vapour Deposition

TLS Tunable Laser Source

TE Transverse Electric

TM Transverse Magnetic

OTDM Optical Time Division Multiplexing

XPM Cross Phase Modulation

XGM Cross Gain Modulation

TOAD Terahertz Optical Asymmetric Demultiplexer

EDFA Erbium Doped Fibre Amplifier

DOL Digital Optical Logic

QW Quantum Well

IID Impurity Induced Disordering

IFVD Impurity Free Vacancy Disordering

OEIC Optoelectronic Integrated Circuit

PIC Photonic Integrated Circuit

PAID Photoabsorption Induced Disordering

SAG Selective Area Growth

EAM Electro-Absorption Modulator

SMZI Symmetric Mach-Zehnder Interferometer

Chapter 1

Introduction

With the constantly increasing demand for bandwidth, an important goal for future optical communication systems, will be the development of Optoelectronic Integrated Circuits (OEICs) [1]. Monolithic integration makes the fabrication of these optical components realistic. The following section describes the advantages and methods of monolithic integration. The work described in this thesis focuses on the simulation and characterization of devices fabricated by a Quantum Well Intermixing (QWI) process. This method provides a practical route to monolithic integration. The potential for achieving more complex functionality is also discussed.

1.1 Monolithic Integration

The primary goals of the monolithic integration of optoelectronic components is to achieve increased functionality in devices at a lower production cost. Photonic systems also simultaneously operate at many wavelengths as opposed to electronics, which are serial in nature. As a result, integration could be even more important to photonics than it ever was to electronics [1].

Most optoelectronic components in use today are manufactured separately. These discrete components are then connected to attain some higher functionality. This method

allows each component to be optimized to perform a single task [2]. Connecting these components however, results in two significant problems. The first is coupling light between chips. This is a dominant source of loss in optoelectronic circuits [3]. The second problem is the cost of packaging each component, which is a large contributor to the production cost [2].

Monolithically integrating these photonic components dramatically reduces the loss due to to coupling, while also providing a significant reduction in the packaging cost. However, all components are now on the same chip, and can no longer be individually optimized. As a result, certain conditions must be met in order to integrate such components successfully. First, although integrated devices may not meet the performance of discrete ones, each component should still work correctly. Secondly, the operation of one component, should not negatively effect that of another [2]. Meeting these two requirements allows the circuit to operate effectively as a whole.

In order for a monolithic integration technique to be successful it should also accomplish certain goals. First, the technique should be practical, not time consuming or costly [2]. And second, the complexity of the process should not increase based on the number of integrated components [2]. Meeting these two goals enables the technique to maintain its cost advantage over discrete components.

A number of monolithic integration techniques have been demonstrated over the past years. These include butt-joint regrowth [4, 5], Selective Area Growth (SAG) [6], and offset quantum wells [7]. In butt-joint regrowth, waveguide core material is selectively etched where it is not required. A new waveguide core is then regrown using a different material. This process is able to integrate devices of different functionality. However, in addition to being time consuming and expensive, it also requires very accurate control over the etch and regrowth material parameters [2].

In the SAG technique the width of the quantum wells are varied during a single epitaxial stage. The substrate has a mask patterned on its surface with slots open on

it. Growth does not take place on the mask, however, the growth species are able to migrate to the nearest opening. The growth rate is dependent on the size of the opening [8]. Several bandedges can be created using this method. However, because the well thickness changes across the wafer, the optical confinement factor cannot be optimized.

With offset quantum wells, the wells are grown above the waveguide and are etched from regions were they are not needed. This process also only requires one growth step and has been used to integrate different components [6]. With offset quantum wells, the mode overlap is not optimized in the well region. The technique is also limited to two band edges [2, 9]. As such it is not suitable for fabricating complex OEICs.

Simple integrated devices have been produced using these methods. However, for complex OEICs, to perform optimally, several bandedges are needed for the various components [1]. For example, in a circuit containing a waveguide, a laser and an Electro-Absorption Modulator (EAM), the waveguide must have a much higher bandedge than the laser to minimize loss. However the EAM should only have a slightly larger bandedge than the laser to achieve low loss and high extinction ratio [3]. As such, a practical technique for integration must be able to practically meet these needs for all of its components.

1.2 Quantum Well Intermixing

A practical technique for monolithically integrating passive and active photonic components would lead to major advancements in information processing. Devices would demonstrate enhanced performance, reliability and lower production cost. QWI is beginning to emerge as a practical method for integrating OEICs. The technique involves the post-growth modification of the bandgap of a Multiple Quantum Well (MQW) system. This is done by intermixing the well and barrier material at high temperatures. The intermixing process causes rounding of the square Quantum Well (QW) profile. This

leads to an increase in the bandgap energy. As a result, optical loss due to absorption is reduced for wavelengths emitted from the non-intermixed regions. Intermixing can be aided by the introduction of impurities or defects near the well/barrier interface. The high mobility of point defects, such as vacancies and interstitials, allows intermixing to occur at considerably lower temperatures. This technique provides a flexible, reliable and cost effective approach compared to other integration schemes.

1.2.1 Review of Techniques

A number of QWI techniques have been developed to help induce intermixing. These include Impurity Induced Disordering (IID), Impurity Free Vacancy Disordering (IFVD), Photoabsorption Induced Disordering (PAID), and ion implantation induced disordering.

With IID, surface dopant diffusion or ion implantation are used to create impurities in the lattice. This results in an increased rate of intermixing during the anneal stage [10]. In MQW systems with low thermal stability, such as, InGaAs-InGaAsP, problems can arise during the anneal. Only a small relative shift in the bandgap between intermixed and non intermixed regions can be produced. Free carrier absorption can also be problematic due to the presence of dopants in the active region [11].

IFVD has been used successfully in GaAs-AlGaAs systems. A dielectric cap is used to promote the diffusion of Ga out of the epilayer during the anneal. This leads to an increase in Ga vacancies which improves the Ga/Al intermixing rate. Selective intermixing can be achieved by using different caps, which either advance or suppress intermixing [12]. Again however, the poor thermal stability of InGaAs-InGaAsP makes it difficult to suppress intermixing, resulting in small differential shifts [11].

In PAID, photons from a laser are absorbed by the quantum wells. Thermal intermixing then results from carrier cooling and non-radiative recombination. Large bandgap shifts result without adversely affecting the optical and electrical characteristics of the material. A gold mask, patterned on the sample, can be used to reflect incident photons

and selectively intermix the material [13]. Diffusion of heat below the mask however, results in poor spatial resolution. [11].

Ion Implantation has been successfully used in many III-V material systems. Point defects are generated in the material through high energy ion implants [3]. However, the technique requires expensive facilities making it quite costly [11].

1.2.2 Plasma enhanced Sputtered SiO2 Technique

AMZIs were produced by our collaborators in Glasgow. They were created by a technique that generates point defects during the deposition of sputtered SiO_2 to enhance intermixing. The technique is impurity free and has simple processing stages making it cost effective [11].

In this intermixing process a thin layer of SiO_2 is deposited on the sample using an RF sputtering machine with an Argon and Oxygen gas mixture. This is followed by a rapid thermal anneal at temperatures between 650-750$°C$ [11].

Investigation of the intermixing process indicated that the sputtering process led to the formation of near surface point defects. In the anneal stage, point defects diffuse toward the sample surface and deeper into the samples. This reduces the defect density in the well region and initiates intermixing, resulting in a blue shifted PL spectrum [11].

Point defects are generated by Argon ions bombarding the sample surface. These ions accelerate from the positively charged plasma to the grounded substrate. As a result they have the energy necessary to break atomic bonds close to the surface. Vacancies and interstitials are created which enhance the interdiffusion of well and barrier species [11].

Intermixing can also be suppressed using a protective capping layer. Photoresist was able to completely stop the intermixing process at 650$°C$. The resist is able to absorb the energy of incoming ions and stop the formation of defects [11].

Being able to produce a range of wavelength shifts across a wafer is also an important

property in fabricating OEICs. This can be accomplished using different methods. The first method is to use multiple sputtering stages, to vary the thickness of the SiO_2 layers across the wafer. In areas with thinner layers the intermixing process is reduced. A second method is to use a Plasma Enhanced Chemical Vapour Deposition (PECVD) SiO_2 capping layer of varied thickness. With this technique only a single sputtering and anneal stage are required [11].

1.3 Thesis Outline

This thesis focuses on the simulation and characterization of a monolithically integrated AMZI using the single step sputtered SiO_2 QWI technique described above.

In Chapter 2, Lumerical's MODE Solutions software was used to simulate the optical characteristics of the AMZI layer structure as well as a new generation layer structure.

In Chapter 3, The design and operation of the AMZI are described. We also present experimental results measuring the transmission spectrum of this integrated device.

In Chapter 4, The functional characteristics of a Symmetric Mach-Zehnder Interferometer are presented. Both its operation as an optical demultiplexer as well as its potential for integration in a circuit to create a binary half adder are discussed.

In Chapter 5, the thesis is concluded with a summary of the important results. The significance of this work as well as potential future directions for further exploration are discussed.

Chapter 2

MODE Simulations of 2D Waveguide Structures

2.1 Introduction

Lumerical's MODE Solutions software is designed to describe the physical operation of both conventional and non-conventional waveguide geometries. The software allows scientists and engineers to quickly simulate their results, enabling them to focus on new design concepts. A new feature to the software is the ability to use a finer mesh in certain regions of the simulation. This enables more accurate simulation of fine structures like the MQW core in the AMZI layer structure, which was not possible with previous versions of MODE.

MODE Solutions was used to simulate the 2D waveguide structure of the AMZI devices as well as a newer generation of layer structure being used presently by our collaborators in Glasgow. These simulations were done to give insight into the optical properties of the structures, such as the modes they support, optimal physical parameters and potential sources of loss. The software is not currently being utilized in the design of intermixed devices. However, incorporating such simulations in the optimization of

future layer structures will allow optimized integrated circuits to be realized. The first simulations done here focus on the as-grown layer structure of the AMZI. This includes the quantum wells as they would be in the active section of the device, without intermixing. Section 2.2.5 however, is focused on the effect intermixing has on the optical properties of the device. Finally a new layer structure that is currently being used in Glasgow is also studied.

2.2 AMZI 2 Dimensional Waveguide

2.2.1 Waveguide Structure

A two dimensional schematic of the waveguide structure used in the AMZIs is shown in figure 2.1.

The material structure is an InGaAs/InAlGaAs MQW heterostructure, grown on an InP substrate. The fabrication of the layer structure is described further in the following chapter. A 2 μm wide ridge was etched 1.6 μm deep into the material structure to provide lateral confinement for waveguiding. The refractive indices of the waveguide layers were calculated using equations derived by Guden and Piprek which modeled the refractive indices of III-V semiconductors at a wavelength of 1550 nm [14]. The imaginary part of the refractive index was not modeled by Guden et al. and was not accounted for in these simulations. As such loss due to absorption is not present in our results. Other material parameters of the waveguide structure are listed in Appendix A. Because these simulations were first approximations of our waveguide structure, changes in the refractive index due to doping and strain were not taken into account. These considerations may be the focus of future simulations.

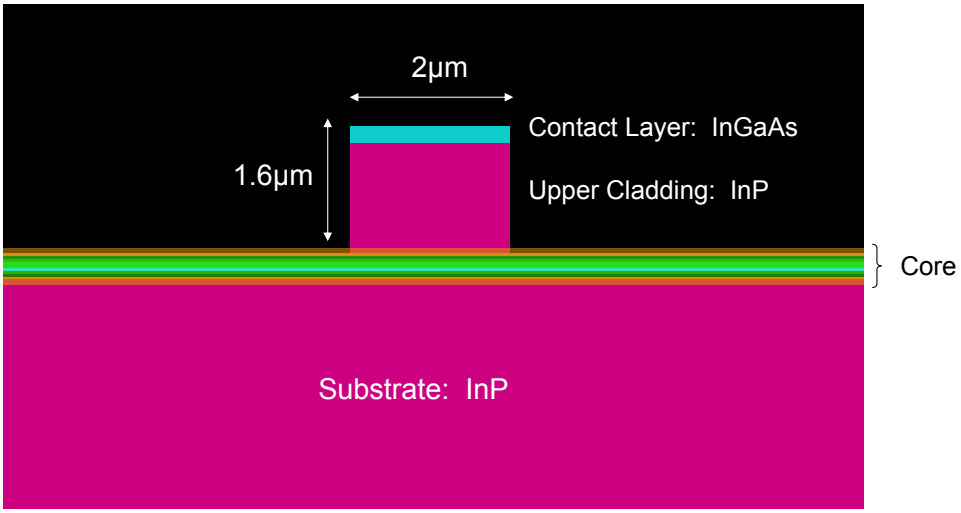

(a)

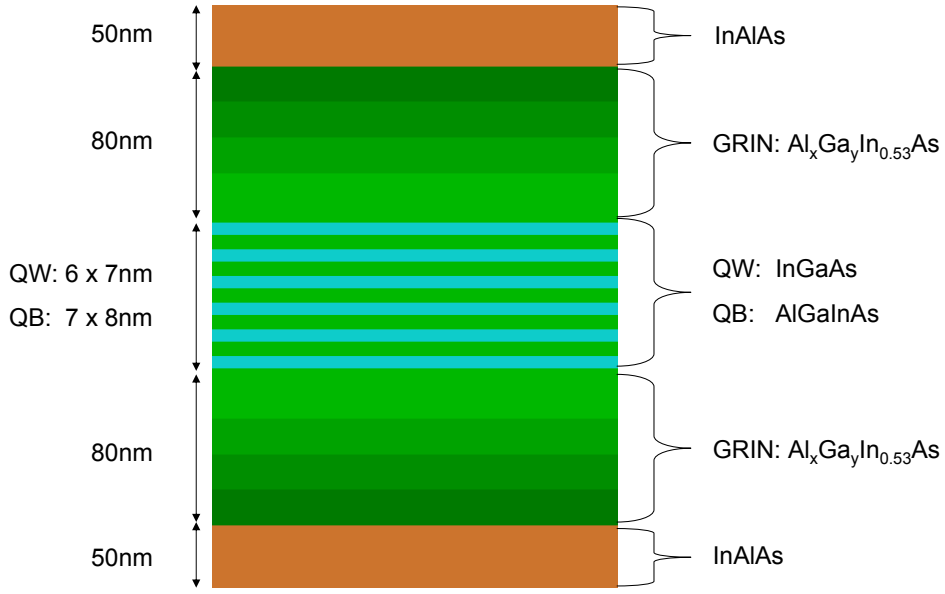

(b)

Figure 2.1: Schematic layout of the (a) AMZI 2 dimensional waveguide structure. (b) an expanded view of the core layer structure.

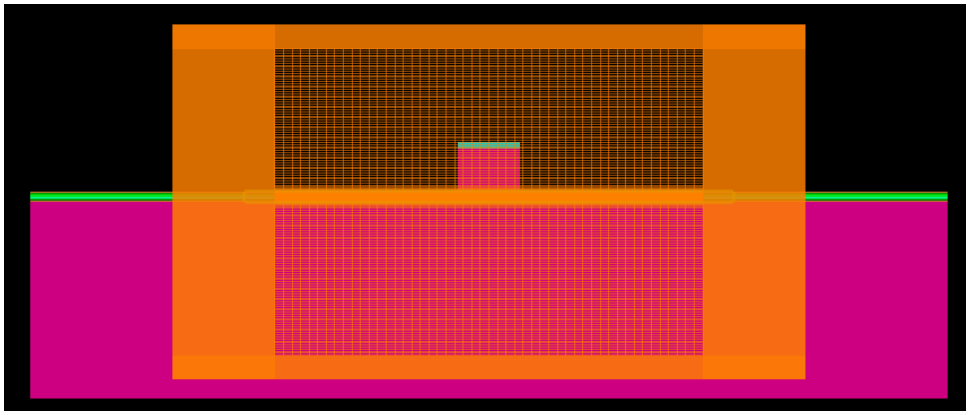

Figure 2.2: Layout of the 2D simulation window defined over the AMZI waveguide structure

2.2.2 Convergence Testing

Before proceeding with detailed simulations of the waveguide structure, convergence testing was carried out. This was done in order to choose the appropriate simulation window and mesh size for the 2 dimensional waveguide structure. Ensuring that convergence is achieved in the measured values allows us to obtain a good level of confidence in the results of our simulations.

To begin with, simulations were done with a coarse mesh over the 2D waveguide structure. Results indicated that a vast majority of the modal E field was centrally located in the core of the waveguide. As such a 14 μm by 10 μm simulation region was centered around the core. A 358 nm high override region was also centered over the core in order to force a finer mesh in that region to resolve the layer structure (figure 2.2).

Next the appropriate number of mesh points and the mesh multiplier for the override region were determined. This was done to make sure convergence was achieved and the simulation didn't take prohibitively long to run. Lumerical's technical support staff suggested a minimum of 3 mesh points for the finest feature of the structure. In the 'x' direction, the number of mesh points was set at 50, so that the 2 μm ridge would be amply resolved. Convergence tests were then done for the effective refractive index as

well as the loss as a function of the number of 'y' mesh points. The 'y' mesh multiplier was left as a parameter. Results of a uniform mesh without an override region were also tracked for comparison (figure 2.3).

Our results indicated that 700 'y' mesh points resulted in simulations which ran in an appropriate time. Convergence of the refractive index and loss had occurred by this point for all the multipliers however, the 100x multiplier converged the fastest. Non-uniform meshes also achieved convergence much faster than uniform ones. The slightly negative values of loss that were observed can be attributed to rounding error. Such low values of loss can be considered 0. In order to make sure that convergence had in fact been achieved, a higher resolution image of the data in the 700 point region was taken (figure 2.4).

Results showed that the 100x 'y' mesh multiplier had in fact converged by 700 'y' mesh points. The increased accuracy in the region where the modes were concentrated is likely why the 100x mesh multiplier showed the best results. A 100x 'y' multiplier with a fixed 700 'y' mesh points was chosen for the remainder of simulations. For 700 'y' mesh points, to meet Lumerical's prescribed 3 points per structure, a multiplier < 103 and > 9.3 is necessary. The multiplier chosen falls well within this range and is thus suitable.

2.2.3 Mode Simulations

Basic Modes

Lumerical's MODE Solutions software was used to simulate the 2D waveguide structure described previously in order to quantify its optical properties. The waveguide was shown to have both first and second order Transverse Electric (TE) modes as well as a first order Transverse Magnetic (TM) mode. The fundamental modes had a TE refractive index of 3.238 and a TM refractive index of 3.222. This is quite different than the refractive index of 3.3 which was used in the design of the AMZI. The mode refractive indices and their

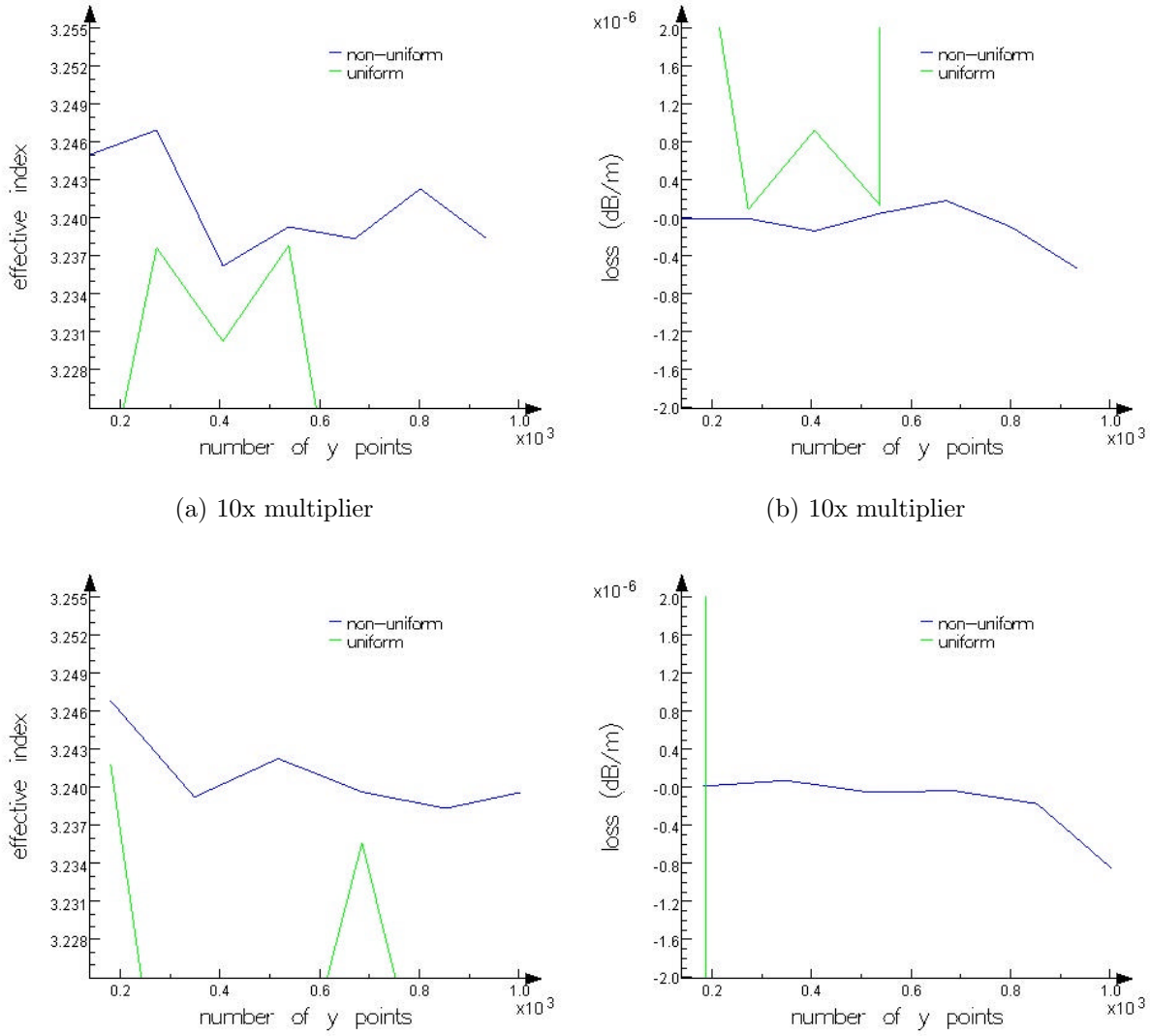

(a) 10x multiplier

(b) 10x multiplier

(c) 20x multiplier

(d) 20x multiplier

Figure 2.3: Convergence of the effective refractive index and loss of the first order TE mode for various y mesh multipliers. Results for both a uniform mesh without an override region as well as a non-uniform mesh with an override region are plotted. (a) n_{eff} for a 10x multiplier. (b) Loss for a 10x multiplier. (c) n_{eff} for a 20x multiplier. (d) Loss for a 20x multiplier.

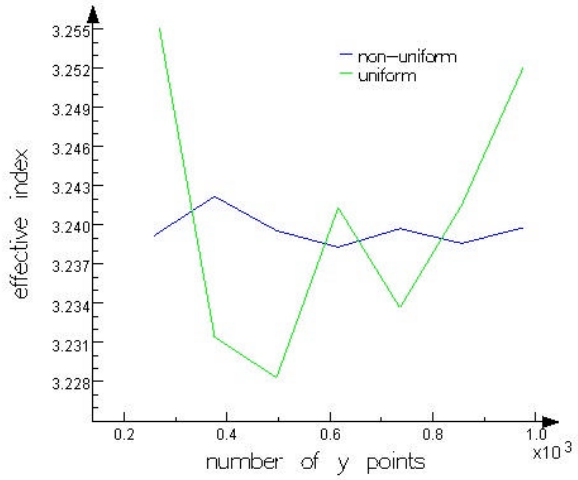

(e) 40x mesh multiplier

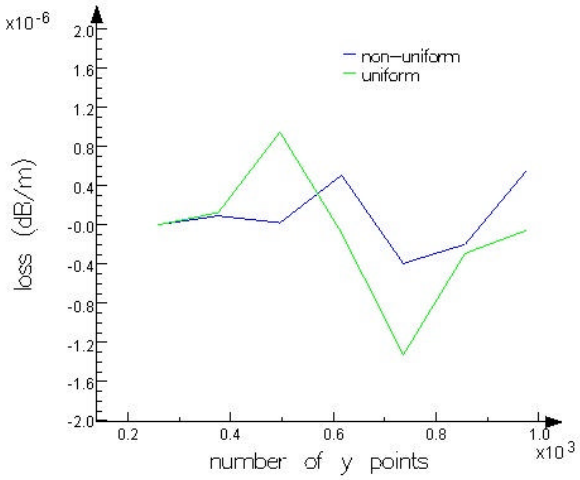

(f) 40x mesh multiplier

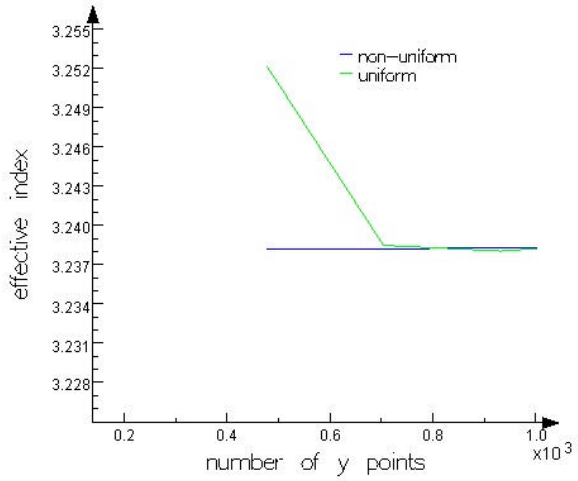

(g) 100x mesh multiplier

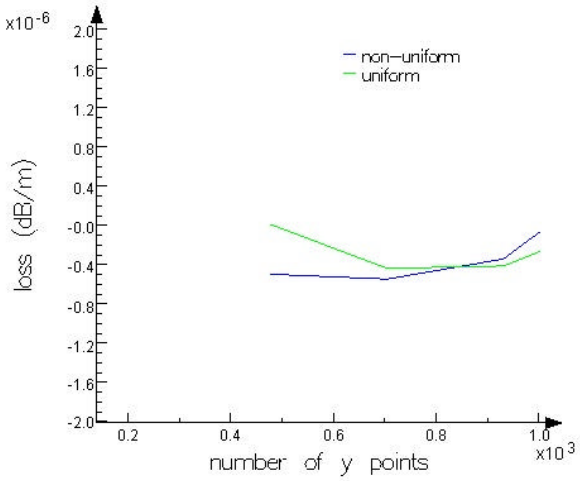

(h) 100x mesh multiplier

Figure 2.3: (cont'd): Convergence of the effective refractive index and loss of the first order TE mode for various y mesh multipliers. Results for both a uniform mesh without an override region as well as a non-uniform mesh with an override region are plotted. (e) n_{eff} for a 40x multiplier. (f) Loss for a 40x multiplier. (g) n_{eff} for a 100x multiplier. (h) Loss for a 100x multiplier.

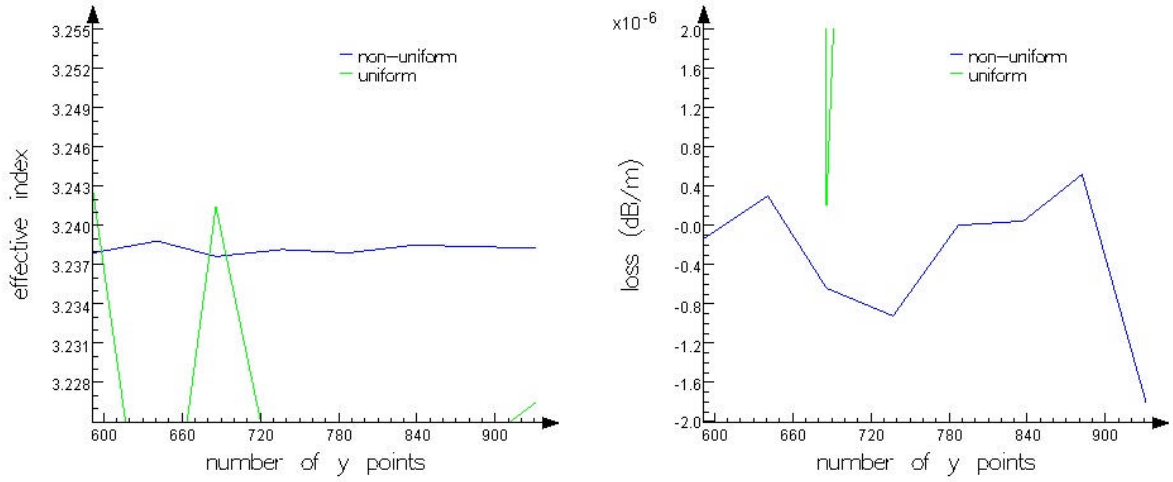

(a) 100x multiplier

(b) 100x multiplier

Figure 2.4: Higher resolution convergence images in the 700 mesh point domain. (a) n_{eff} for a 100x multiplier. (b) Loss for a 100x multiplier.

Table 2.1: Simulated modes of AMZI Waveguide Structure

Mode	Refractive Index	Loss (dB/cm)
First Order TE	3.238	1.785e-9
First Order TM	3.222	2.348e-9
Second Order TE	3.207	9.566e-5

associated losses are listed in table 2.1.

Circular Nature

Another aspect that is important to the application of these devices is the coupling of a standard optical fiber to the waveguide. The fundamental mode of a fiber is circular and often larger than that of the waveguide mode. This mismatch generally results in significant losses. Although a fiber's output can be focused through tapers and lenses, generally the field is still circular. This fact makes the circular nature of a waveguide mode an important element in its design. The radius of our fundamental TE mode was

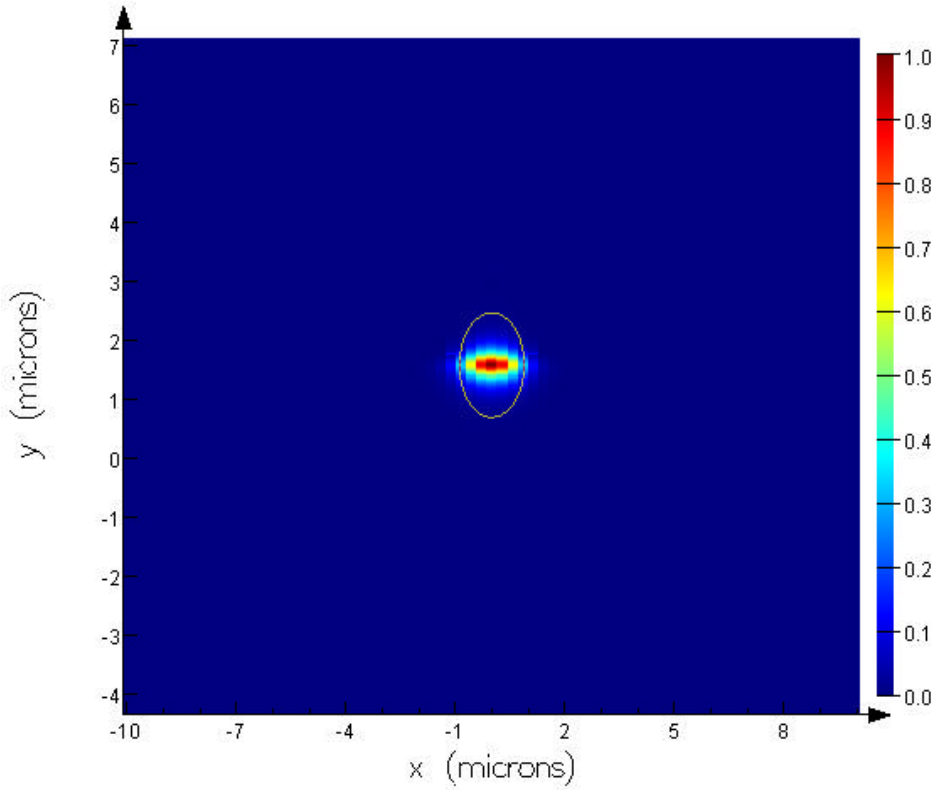

Figure 2.5: Fundamental TE mode overlayed with the outline of a Gaussian mode of the same radius, 886 nm

determined to be 886 nm. An overlap analysis was done with a Gaussian mode of the same radius. An overlap of 81.7% between the two modes was achieved (figure 2.5). This indicated that the fundamental mode of the waveguide was indeed quite circular as would be required for good fiber coupling.

2.2.4 Ridge Width Analysis

Many parameters such as layer dimensions, refractive indices and lateral patterning, determine the number, shape and confinement of guided modes in a waveguide structure. The ridge width, is one parameter that could easily be changed in mask designs and is the first dimension we chose to analyze.

Strip loaded waveguide geometries are often used to achieve lateral confinement in III-

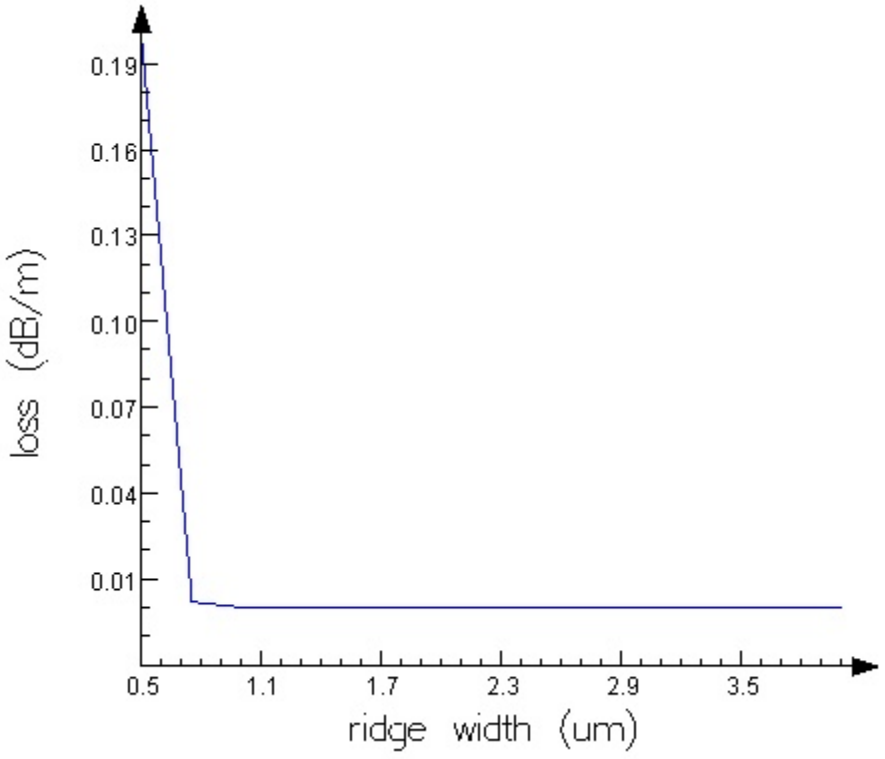

Figure 2.6: Loss as a function of ridge width for the AMZI layer structure

V semiconductor waveguides. Narrow ridges generally result in single mode structures. However high optical loss can result due to the lack of confinement in the horizontal direction. Wide ridges generally lead to better confinement. These structures though, can be multimoded, which also leads to a lack of power in the fundamental mode. To determine the optimal ridge width of the waveguide structure, simulations were carried out to calculate the loss of fundamental modes for various ridge widths. The results are shown in figure 2.6.

The loss of the first order TE mode is lowest above 1 μm ridge widths. Below about 0.8 μm the loss increases drastically. Second order modes were only observed at ridge widths above 1.5 μm. Above 3 μm the device begins to guide even higher order modes.

2.2.5 Intermixed Structure

Thus far our simulations have been carried out on a layer structure which was modeled after an unintermixed portion of the AMZI. However as discussed in the introduction, intermixing causes a rounding of the initially square QW profile, which leads to an increase in the bandgap energy. This would in turn lead to a change in the effective refractive index of the core section. In the AMZIs, the vast majority of the device is passive and therefore intermixed. Only the active Semiconductor Optical Amplifiers (SOAs) remained unintermixed. Traditionally intermixed devices are designed based on the active layer structure, which has been optimized for laser operation. If however, the refractive index change due to intermixing is significant, it would make more sense to design devices based on the intermixed optical properties, rather than the active ones.

Intermixed Wells and Barriers

To test this hypothesis, simulations were carried out on an intermixed structure. In order to approximate an intermixed structure the MQW core of our previous 2D structure was replaced with a single layer. The TE and TM refractive index of this layer was calculated using equations (2.1) and (2.2) respectively. These equations were taken from the form-birefringence description of Suzuki et al. which was developed further by Kleckner et al. [15, 16]. The TE refractive index was 3.516 where as the TM refractive index was 3.533.

$$n_{TM} = \left(\frac{t_A n_A^2 + t_B n_B^2}{t_A + t_B} \right)^{1/2} \tag{2.1}$$

$$n_{TM} = \left(\frac{n_A^2 n_B^2 (t_A + t_B)}{n_B^2 t_A + n_A^2 t_B} \right)^{1/2} \tag{2.2}$$

This method takes a weighted average of the refractive index of each layer. Taking such an average implies that the entire core is completely mixed. However simulations of such a structure will still provide us with insight into the effect of well and barrier

Table 2.2: Simulated fundamental modes of the Intermixed core of the AMZI Waveguide Structure

Mode	Refractive Index	Loss (dB/cm)
First Order TE	3.238	9.3647e-9
First Order TM	3.226	5.505e-10

Table 2.3: Simulated fundamental modes of the Intermixed core and GRIN layers of the AMZI Waveguide Structure

Mode	Refractive Index	Loss (dB/cm)
First Order TE	3.229	1.75e-9
First Order TM	3.217	1.606e-8

mixing on the device's optical properties.

The results of the simulations are displayed in table 2.2.

When compared with the results listed in table 2.1, it is clear that averaging the quantum wells/barriers did not have a significant effect on the effective refractive indices of the fundamental modes.

Intermixed GRIN Layers

In addition to intermixing taking place in the MQW core structure, it also has the effect of intermixing the Graded Refractive Index (GRIN) layers in figure 2.1b. This effect was approximated by replacing the step-like GRIN structure with one in which the refractive index was varied linearly. Simulations were again carried out, the results of which are listed in table 2.3

These results indicate a larger change to the refractive index than those of just the intermixed wells/barriers. However the change is still not a very large difference when compared with the results of the active structure in table 2.1.

Fresnel Reflection Loss

As a measure of how significant the change in refractive index was in the intermixed structure we looked at the Fresnel reflection loss of light passing from an intermixed section of the device to an active region. The value obtained was $R = 1.94\text{x}10^{-6}$, which corresponds to a $8.43\text{x}10^{-6}$ dB loss. This is a very insignificant loss.

Since a true intermixed material profile is closer to that of the active layer structure than to that of the averaged structure we chose to continue using the active layer structure for simulations.

2.3 AMZI Sources of Loss

2.3.1 Fiber Coupling Loss

The fundamental mode of a fibre is circularly symmetric and often large compared with that of the waveguide. The mismatch that results often leads to significant losses, as was mentioned previously. The coupling efficiency between an SMF-28 optical fibre and our waveguide structure is given by the square of the overlap between the fibre and waveguide modes. Corning SMF-28 optical fiber has a circular mode profile with a radius of 5.2 μm. It also has an effective refractive index of 1.4682. MODE Solutions was used to carry out the overlap analysis between the waveguide's fundamental TE mode, which had a radius of 886 nm, a Gaussian mode of radius 5.2 μm and refractive index of 1.4682. The two profiles are shown in figure 2.7.

The power coupling efficiency was determined by Mode to be only 7.36%. This corresponds to a 11.3 dB loss. As a result a tapered or lensed fibre would be required to focus the fibre's mode and increase coupling.

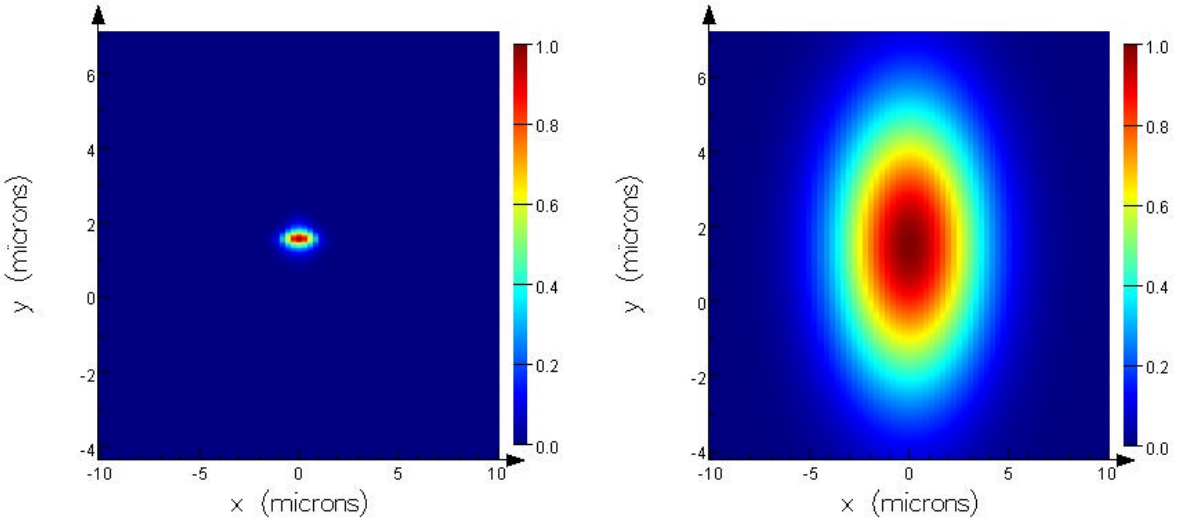

(a) (b)

Figure 2.7: Mode profiles of the (a) fundamental TE mode. (b) SMF-28 Fibre mode.

2.3.2 Fresnel Reflection Loss

Another potential source of loss for such a device is Fresnel reflection loss. This is due to the reflection that occurs when light passes from one medium to another of different refractive indices. The Fresnel reflection coefficient was calculated between air and the waveguide for free space coupling, as well as between the fibre and the waveguide for fiber butt coupling. The values obtained were $R = 0.28$ and $R = 0.14$ respectively. This corresponds to a loss of 1.44 dB for free space coupling and 0.66 dB for fibre butt-coupling. These losses would need to be compounded at both interfaces of the device. These losses could easily be reduced by the application of an anti-reflection coating, or by coupling into the device at the the Brewster angle.

2.3.3 Bend Loss

There are two main types of loss in curved waveguides, pure bend loss, which arises from the bent section of a waveguide, and transition loss that occurs at the discontinuity

between a straight and curved waveguide. Both types of loss can be minimized with careful choice of device parameters.

Pure Bend Loss

Bending of a single mode waveguide leads to the attenuation of optical power in the fundamental mode as it propagates. This attenuation is due to the radiation loss from modal field in the cladding [17].

An approximate expression for pure bend loss was used by Ladoucer et al. and is given by equation (2.3).

$$\alpha = \frac{1}{k_o n_{eff} \rho^2} \frac{U^2 W^2}{1+W} exp(2W) exp\left(-\frac{4W^3 \Delta R_c}{3V^2 \rho}\right) \tag{2.3}$$

Where $V = k_o \rho n_{co} \sqrt{\frac{n_{co}^2 - n_{cl}^2}{n_{co}^2}}$, $U = k_o \rho \sqrt{n_{co}^2 - n_{eff}^2}$, and $W = k_o \rho \sqrt{n_{eff}^2 - n_{cl}^2}$. R_c is the radius of curvature, n_{cl} is the cladding refractive index, n_{co} is the core refractive index, and k_o is the free space wavenumber. From this expression bend loss can be minimized by selecting an appropriate radius of curvature. MODE Solutions was used to determine the loss of the the fundamental TE mode of the waveguide for various radii of curvature. The results are depicted in figure 2.8.

Optical Loss is lowest above a radius of 400 μm, however below 400 μm the loss begins to increase significantly.

Transition Loss

Modal mismatch between straight and continually curved waveguides can also cause radiation loss. This type of loss can be minimized by introducing an offset between the straight and curved sections in order to achieve maximum overlap between the two fields. In order to determine the appropriate offset for the curved sections of our waveguides, MODE was used to carry out an overlap analysis between the fundamental TE modes of a straight waveguide and one with radius of curvature of 600 μm. The analysis indicated

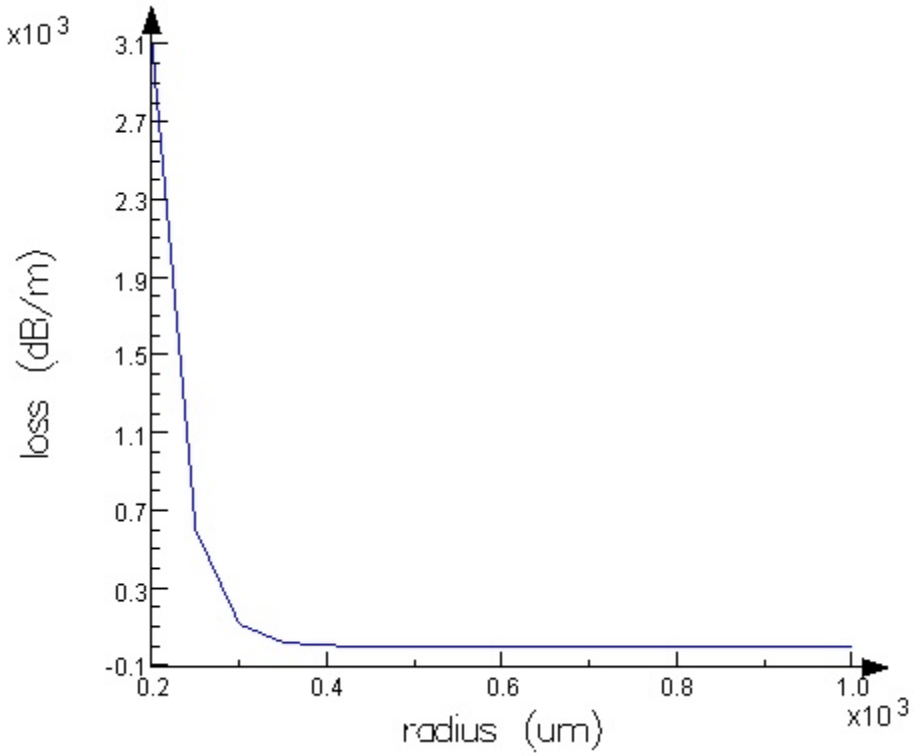

Figure 2.8: Loss as a function of bend radius for the AMZI layer structure

a 98.9% overlap between the two fields and indicated that only a 20 pm offset was necessary in order to optimize this overlap. This small offset is likely due to the index contrast between the ridge and cladding region, which were found to be 3.25 and 3.19 respectively. Based on these simulation we can exclude transition offset as a potential source for improving device functionality.

2.4 New Layer Structure 2 Dimensional Waveguide

Recently our collaborators at the University of Glasgow have been working with a new layer structure, which they deem to be a better candidate for QWI optical devices. Although we were unable to get devices made with this layer structure for characterization, we decided to simulate the waveguide structure as an approximation of its optical properties. This will give us some indication of whether or not it is in fact a more appropriate structure.

2.4.1 Waveguide Structure

A two dimensional schematic of the new waveguide structure is shown in figure 2.9.

The material structure is an InAlGaAs MQW heterostructure, grown on an InP substrate. A 2 μm wide ridge was etched 1.85 μm deep into the material structure. The refractive indices of the layers which were used in the simulations were calculated at a wavelength of 1550 nm based on a paper by Guden et al. [14]. More details on the material structure are provided in Appendix A.

2.4.2 Convergence Testing

A convergence test was again carried out on the structure. This time a 420 nm override region was used to force a finer mesh around the core. 50 'x' mesh points were used to resolve the 2 μm wide ridge. The 'y' mesh multiplier was again left as a parameter. The

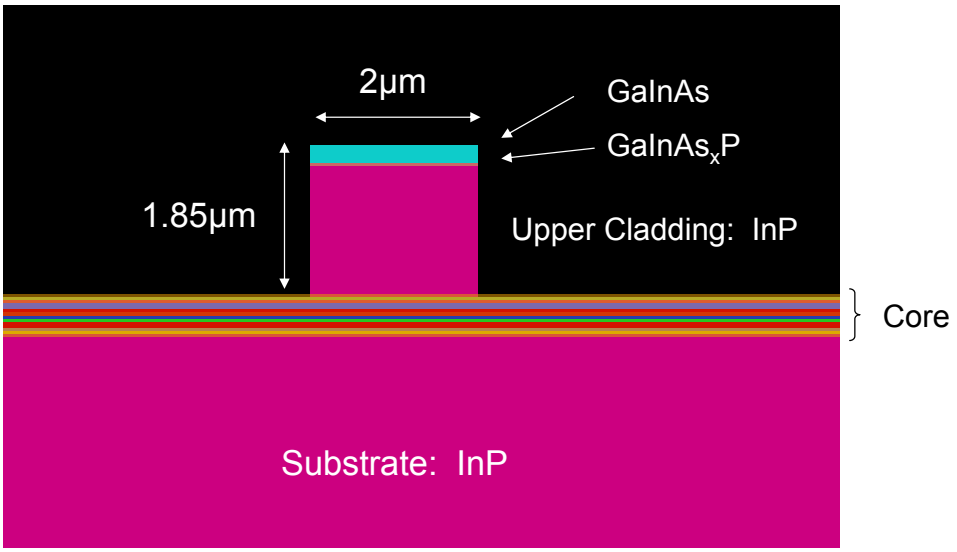

(a)

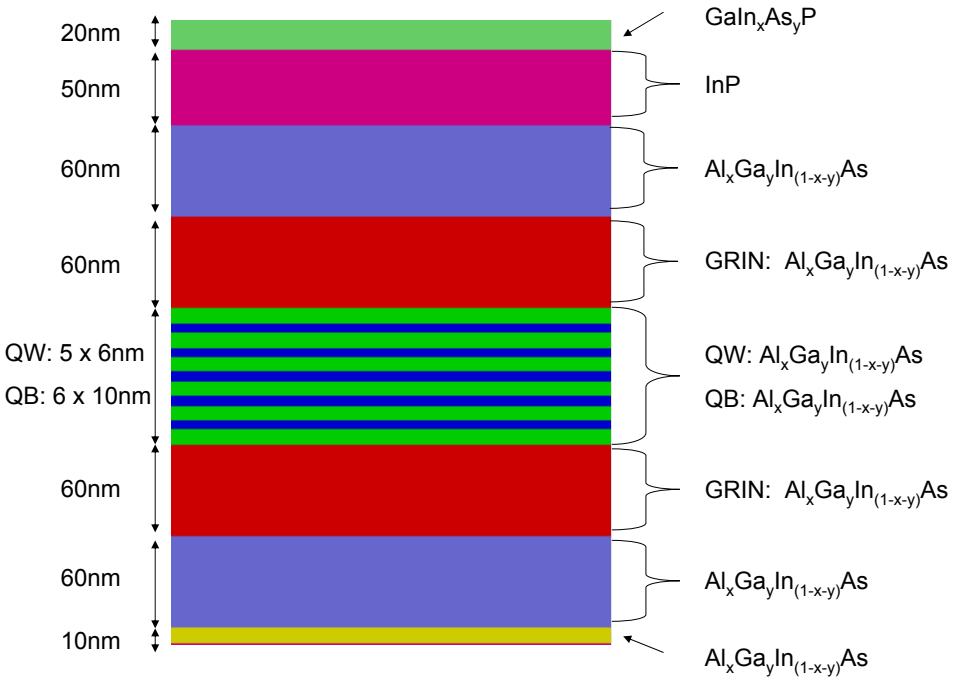

(b)

Figure 2.9: Schematic layout of the (a) New layer structure 2 dimensional waveguide. And (b) expanded view of the core.

Table 2.4: Simulated modes of New Layer Waveguide Structure

Mode	Refractive Index	Loss (dB/cm)
First Order TE	3.222	7.752e-8
First Order TM	3.213	7.296e-7
Second Order TE	3.196	0.255

results for a the 90x multiplier are shown in figure 2.10.

The 90x 'y' mesh multiplier showed the best convergence. It too was closest to the upper bound for the mesh multiplier as in the previous simulations. However, 800 total 'y' mesh points were chosen for the simulation window, as convergence seemed to occur by this point.

2.4.3 Mode Simulations

Basic Modes

Again Lumerical's MODE Solution's Software was used to simulate the 2D waveguide structure. As with the AMZI layer structure, this waveguide was found to have both first and second order modes. The fundamental mode had a TE refractive index of 3.222 and a TM refractive index of 3.213. The modes refractive indices and their corresponding losses are listed in table 2.4.

Circular Nature

The radius of the fundamental TE mode was determined to be 943 nm. An overlap analysis was done with a Gaussian mode of the same radius. An 83.7% overlap between the two modes was achieved (figure 2.11). Although the size of the mode is slightly larger than that of the AMZI structure, there was not a significant change. The mode was also only slightly more circular than what was previously determined for the AMZI.

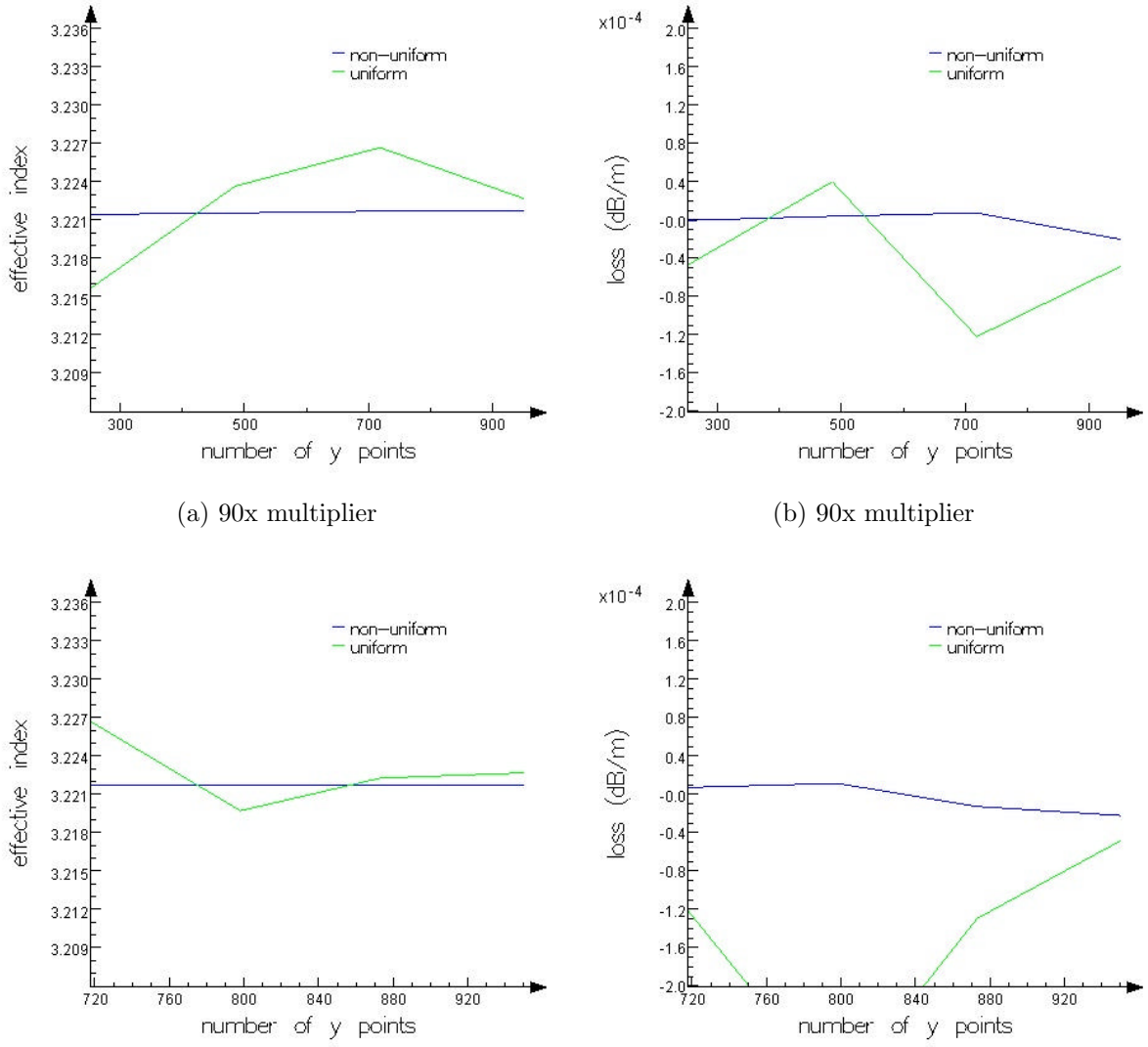

(a) 90x multiplier

(b) 90x multiplier

(c) 90x multiplier

(d) 90x multiplier

Figure 2.10: Convergence of the (a) effective refractive index and (a) loss of the first order TE mode for a 90x 'y' mesh multipliers. Higher resolution in the 800 mesh point domain. (c) n_{eff} for a 90x multiplier. (d) Loss for a 90x multiplier.

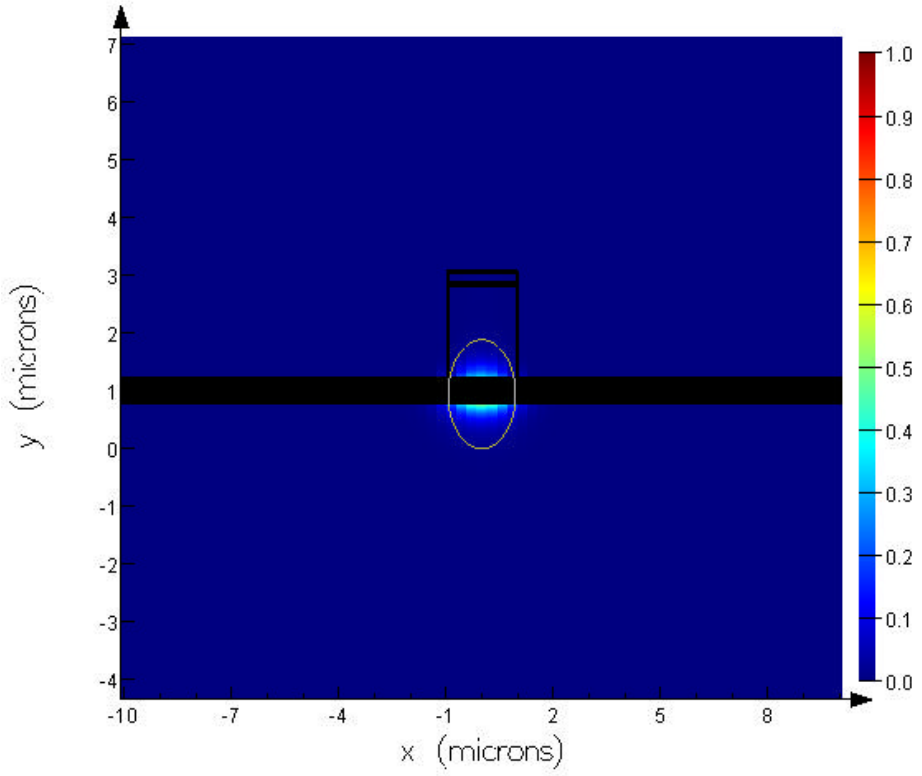

Figure 2.11: Fundamental TE mode overlayed with the outline of a Gaussian mode of the same radius, 943 nm

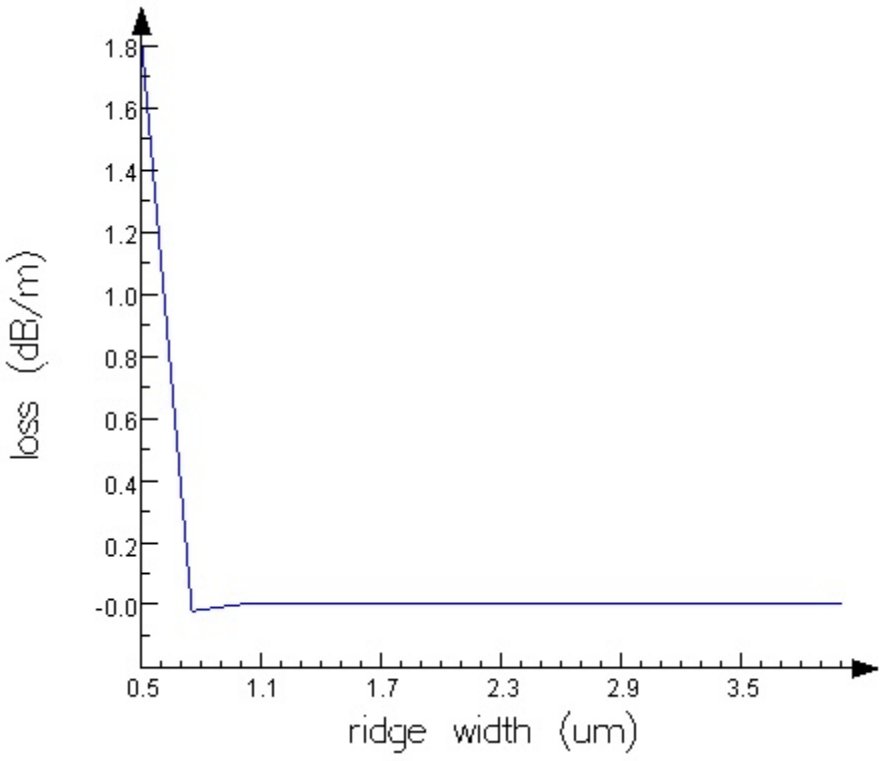

Figure 2.12: Loss as a function of ridge width for the new layer structure

2.4.4 Ridge Width Analysis

In order to determine the optimal ridge width for a device made from this layer structure, simulations were carried out at various ridge widths. The loss as a function of ridge width for the fundamental TE mode is plotted in figure 2.12.

The lowest loss was observed at a ridge width above 1 μm. Below 0.8 μm the loss increases rapidly as more of the mode is found in the cladding. Above 1.5 μm second order modes begin to propagate in the structure. At greater than 3 μm even higher order modes were observed.

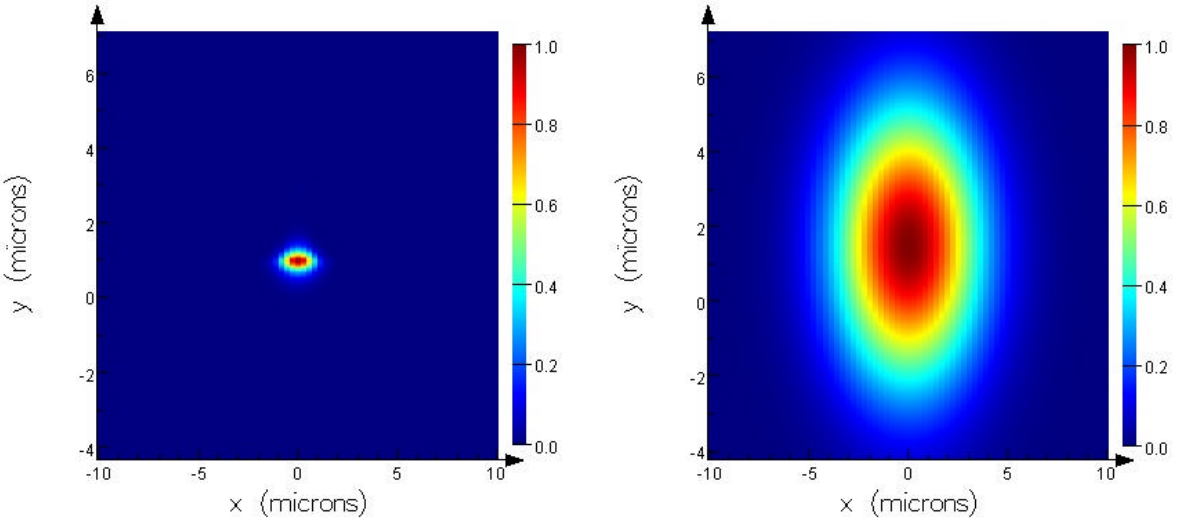

(a) (b)

Figure 2.13: Mode profiles of the (a) fundamental TE mode. (b) SMF-28 Fibre mode.

2.5 New Layer Structure Sources of Loss

2.5.1 Fiber Coupling Loss

In order to determine the fiber coupling loss, MODE Solutions was used to carry out an Overlap Analysis between a Gaussian mode of radius 5.2 μm with an effective refractive index of 1.4682, and the fundamental TE mode of the waveguide structure. The power coupling efficiency was determined by mode to be 9.2%. This is slightly higher than the coupling efficiency of the AMZI structure, and is the result of the slightly larger mode that was observed previously. The coupling efficiency corresponds to a 10.4dB loss. As such, fibers with a taper or lens to focus the mode would be necessary for coupling. The two mode profiles are shown in figure 2.13

2.5.2 Fresnel Reflection Loss

The Fresnel reflection coefficient was calculated between air and the waveguide for free space coupling, as well as between the fibre and the waveguide for fiber butt coupling.

The values obtained were again $R = 0.28$ and $R = 0.14$ respectively. This corresponds to a loss of 1.44 dB for free space coupling and 0.66 dB for fibre butt-coupling. Again these losses would need to be compounded at both interfaces of the device, and could be minimized by the application of an anti-reflection coating.

2.5.3 Bend Loss

Pure Bend Loss

As with the AMZI structure MODE Solutions was used to determine the loss of the the fundamental TE mode of the waveguide for various radii of curvature. The results are shown in figure 2.14. Optical Loss is lowest at a radius above 700 μm, however below 600 μm the loss begins to increase dramatically. This is a significant increase in the bend radius, than what was observed for the AMZI structure, where loss increased dramatically below 400 μm.

Transition Loss

In order to determine the appropriate offset for the curved sections of our waveguides, MODE was used to carry out an overlap analysis between the fundamental TE modes of a straight waveguide and one with radius of curvature of 600 μm. The analysis indicated a 98% overlap between the two fields and indicated that a 460 pm offset was necessary in order to optimize this overlap. This offset is again not significant enough to improve the design of devices made in this layer structure.

2.6 Conclusion

The optical properties of the AMZI Layer structure as well as the new generation of layer structure were studied. The effective refractive index of the AMZI layer structure was found to be 3.238, which is different from that which was used in its design, 3.3.

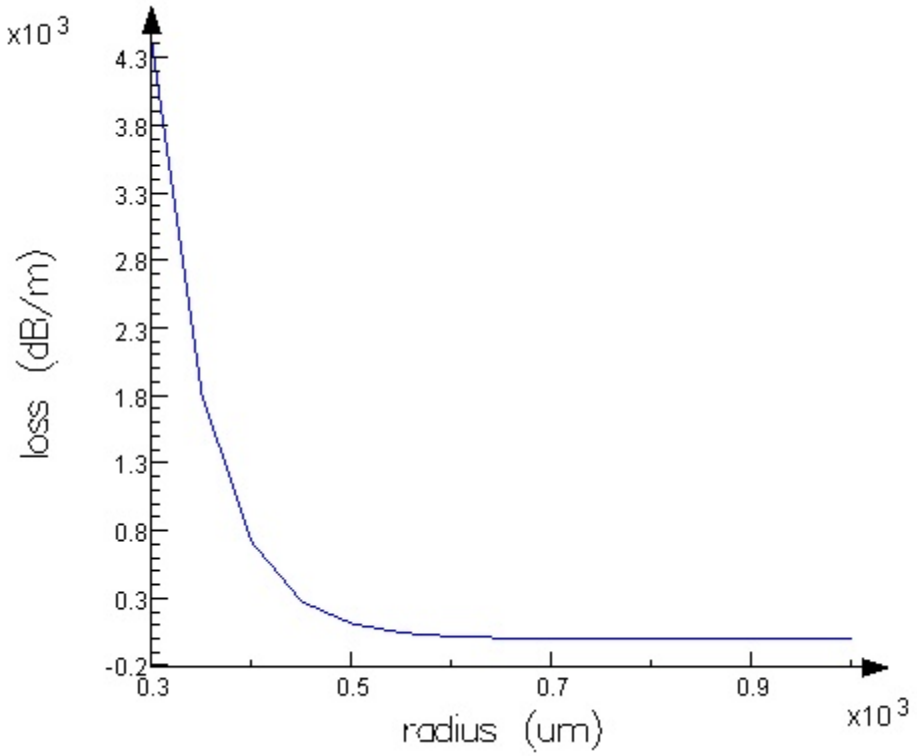

Figure 2.14: Loss as a function of bend radius for the new layer structure

Not many difference between the AMZI and new layer structure were observed. Both structures had second order modes. The most significant source of loss was due to the coupling efficiency between a fiber and the structure. A ridge width between 1-1.5 μm, was ideal for both structures. For the AMZI structure a bend radius above 400 nm was necessary to minimize loss, where as for the new layer structure this increased to 700 nm. An 'intermixed' structure in which the active layers were replaced with an averaged layer was also simulated. Very little change to the refractive index was observed. Simulations such as these would be very useful in the optimization of future layer structures and devices that are produced by our collaborators in Glasgow.

Chapter 3

Asymmetric Mach Zehnder Interferometer

3.1 Literature Review

Wavelength Division Multiplexing (WDM) has begun to emerge as the best way of increasing the transmission capacity and flexibility of optical telecommunication systems. As a result, research is being focused on the development of these WDM systems to meet the need for increased network capacity. Wavelength Multiplexer/Demultiplexers (mux/demuxs) and wavelength selective routers are key devices in such systems [18]. The tunability of these devices is also important as it allows for proper matching of the system wavelength. AMZIs have been shown to be a simple and versatile way of achieving this functionality [18–21].

Integrated AMZIs for mux/demux applications as well as wavelength filters have been demonstrated in a number of different materials. Among these is the Silicon on Insulator (SOI) material system. Tuning of these devices has traditionally been done via the thermo-optic effect [22, 23]. Hoshi et al. however, have also demonstrated switching using a Ferroelectric Liquid Crystal (FLC) cladding in one arm of the interferometer. The

refractive index of the FLC can be changed based on the polarity of an applied voltage, thereby varying the optical path length difference between the two interferometer arms and changing the interference condition [21]. SOI based devices offer the potential for low cost as they are able to take advantage of conventional Complementary Metal-Oxide Semiconductor (CMOS) manufacturing technology. However, the indirect bandgap of silicon makes the monolithic integration of active and passive components very difficult [24].

AMZIs have also been demonstrated in III-V bulk semiconductors such as In-P based devices [20, 24]. Tunability is achieved via the electro-optic effect. Active components can be monolithically integrated in these devices. This leads to a size reduction and lower production costs for complex devices [24]. Studenkov et al. were able to monolithically integrate active and passive components in a Mach-Zehnder Terahertz Optical Asymmetric Demultiplexer (MZ-TOAD) using a twin waveguide structure [25]. The upper active layer was a multiple quantum well stack used to produce optical gain (ie. an SOAs), where as the lower passive layer was used for waveguides. Light is coupled between the two layers using tapered couplers. Monolithically integrated AMZIs as add/drop multiplexers have also been demonstrated in the InP/InGaAsP material system [26]. All Optical Wavelength conversion by a monolithically integrated AMZI was also achieved in this material system using buried stripe loaded technology [27]. The tunability of this device however was not demonstrated. Devices in this bulk III-V semiconductor system generally exhibit higher propagation and fiber coupling loss [24].

Devices that are made with III-V semiconductor quantum well structures are able to utilize the large electorefraction effect to achieve phase changes. Secondly, it is also possible to monolithically integrate various components on a single chip through QWI which is a high yield, cost effective device integration technique as was described previously. Our interest in the AMZIs stemmed from these characteristics. As such, characterization of these devices was carried out to aid in the design and fabrication of future monolithically

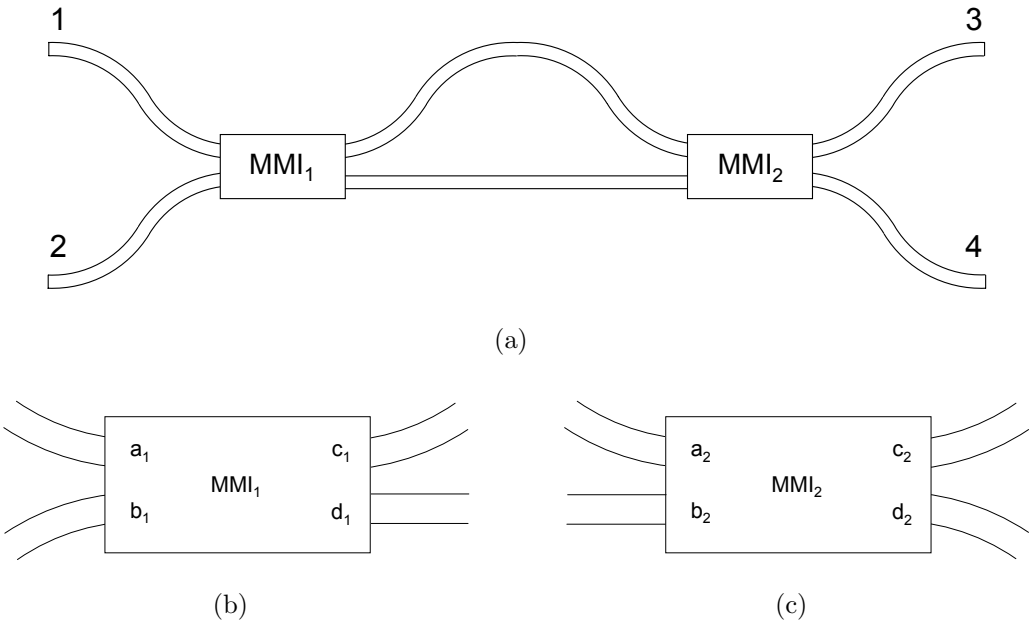

Figure 3.1: (a) Schematic layout of the integrated AMZI. (b) Expanded schematic of MMI_1 (c) Expanded schematic of MMI_2

integrated devices.

3.2 Background

A Mach-Zehnder interferometer is a device that works based on the interference of two optical beams. A single beam is split into two by a beam splitter. Each beam is then exposed to a different optical path length that arises from a length or refractive index difference. This results in each beam accumulating a different amount of phase. The two beams are then recombined through a second beam splitter. The relative phase difference between the two beams results in either constructive or destructive interference, leading to a distribution of power between the two output ports [28].

The monlithically integrated Mach-Zehnder interferometer described here is composed of a 2x2 Multimode Interference (MMI) coupler followed by two interferometer arms of different optical path lengths which lead into a second 2x2 MMI coupler (figure 3.1).

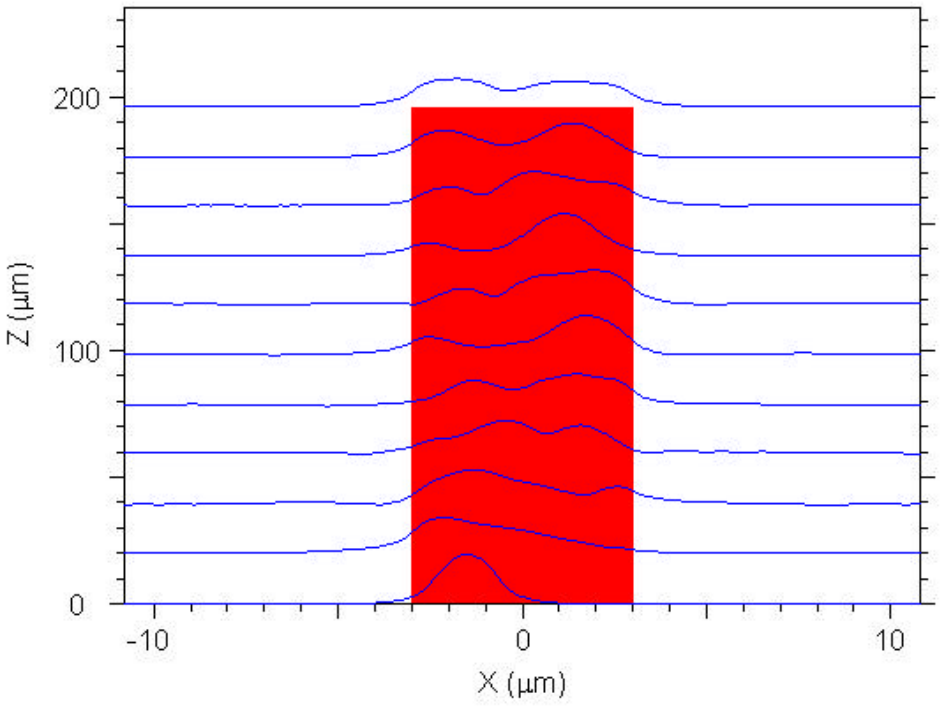

Figure 3.2: RSoft Simulation of a 6x196 μm MMI made from the new layer structure described in the previous chapter

Self imaging is the fundamental principle behind an MMI coupler. The input field in a multimode waveguide is reproduced in single and multiple images at periodic distances along the waveguide [29, 30]. Single mode waveguides are used to couple light into and out of the MMI. Based on interference principles for a multimode waveguide, two symmetric images of the input field are produced at a distance of $2n_rW_e^2/\lambda_o$ from the input, where n_r is the ridge effective refractive index, λ_o is the free space wavelength of the input light, and W_e is the effective width of the fundamental mode [30]. A simulation of a 6x196 μm MMI fabricated in the new layer structure described in Chapter 2 is shown in figure 3.2. The single mode input is converted into 2 modes at the output, over the length of the device.

If light was coupled into input port a_1 of the MMI in figure 3.1b, the two images would be at positions c_1 and d_1. The image at position c_1 would be a direct copy of the input field with half the amplitude. The image at position d_1 would also have half the

amplitude of the input field however, it would be a mirror image of the field at position c_1. The field at position d_1 would also have a phase difference of $\pi/2$ with respect to that at position c_1. Similarly if light was coupled into input port b_1 of the MMI, two images of this field would also be obtained at positions c_1 and d_1. Each image would now have the opposite orientation and phase as that explained above [29, 30]. The 2x2 3dB couplers used in our devices also function in this way. The relationship between input and output fields of these 2x2 MMI couplers can be described by the following equation [29],

$$\begin{aligned}\begin{bmatrix} E_{out}(c_1) \\ E_{out}(d_1) \end{bmatrix} &= \begin{bmatrix} M_{MMI} \end{bmatrix} \begin{bmatrix} E_{in}(a_1) \\ E_{in}(b_1) \end{bmatrix} \\ &= \frac{1}{\sqrt{2}} \begin{bmatrix} 1 & e^{j\pi/2} \\ e^{j\pi/2} & 1 \end{bmatrix} \begin{bmatrix} E_{in}(a_1) \\ E_{in}(b_1) \end{bmatrix}\end{aligned} \tag{3.1}$$

The phase shift that is introduced by the upper and lower interferometer arms is βl_{upper} and βl_{lower} respectively, where $\beta = 2\pi n_{eff}/\lambda$. n_{eff} is the effective refractive index, λ is the free space wavelength and l_{upper} and l_{lower} are the lengths of the upper and lower interferometer arms respectively. For convenience we only take into account the relative phase shift of the upper arm $\beta\Delta L$, where $\Delta L = l_{upper} - l_{lower}$. The matrix describing the input and output relationship of the interferometer arms becomes [19],

$$\begin{aligned}\begin{bmatrix} E_{out}(a_2) \\ E_{out}(b_2) \end{bmatrix} &= \begin{bmatrix} M_{Interferometer} \end{bmatrix} \begin{bmatrix} E_{in}(c_1) \\ E_{in}(d_1) \end{bmatrix} \\ &= \begin{bmatrix} e^{j\beta\Delta L} & 0 \\ 0 & 1 \end{bmatrix} \begin{bmatrix} E_{in}(c_1) \\ E_{in}(d_1) \end{bmatrix}\end{aligned} \tag{3.2}$$

To see how the interferometer works we can follow the phase accumulated by light entering input port 1 of figure 3.1 and traversing the device on the way to the output ports.

The lower path picks up the following phase shifts on it's way to output port 3. $\pi/2$ relative phase change going through MMI_1, zero relative phase change going through the lower interferometer arm, and $\pi/2$ relative phase change going through the second MMI_2. This gives a total of,

$$\pi/2 + \pi/2 = \pi \tag{3.3}$$

The upper path also on it's way to output port 3, picks up zero phase change at MMI_1, $2\pi n_{eff}\Delta L/\lambda$ going through the upper interferometer arm, and zero relative phase change going through MMI_2. The phase difference between the two paths is

$$2\pi \mathrm{n}_{eff}\Delta L/\lambda - \pi = \beta\Delta L - \pi \tag{3.4}$$

Similarly we can calculate the phase difference between the two paths on their way to output port 4.

$$2\pi \mathrm{n}_{eff}\Delta L/\lambda + \pi/2 - \pi/2 = \beta\Delta L \tag{3.5}$$

If $\Delta L = 0$ there is destructive interference at output port 3 and constructive interference at output port 4. By varying $\beta\Delta L$ from 0 to π, the probability of light arriving at either output port can be varied from 0 to 1. This can be achieved by varying the optical path lengths of the interferometer arms. The same relationships would result for the bar and cross ports if light were to be coupled into input port 2 instead of 1 [31].

The relationship between input and output fields of the AMZI can be found by multiplying the matrices for both 3dB couples and the interferometer arms [19],

$$\begin{bmatrix} E_{out}(3) \\ E_{out}(4) \end{bmatrix} = \begin{bmatrix} M_{MMI} \end{bmatrix} \begin{bmatrix} M_{Interferometer} \end{bmatrix} \begin{bmatrix} M_{MMI} \end{bmatrix} \begin{bmatrix} E_{in}(1) \\ E_{in}(2) \end{bmatrix}$$
$$= \begin{bmatrix} -1 + e^{j\beta\Delta L} & j(1 + e^{j\beta\Delta L}) \\ j(1 + e^{j\beta\Delta L}) & 1 - e^{j\beta\Delta L} \end{bmatrix} \begin{bmatrix} E_{in}(1) \\ E_{in}(2) \end{bmatrix} \tag{3.6}$$

An Important design parameter for an AMZI is it's extinction ratio. This extinction ratio is dependent on the power imbalance at the input ports of the second MMI. The imbalance results from differing loss in the asymmetric interferometer arms as well as irregularities in the splitting ratio of the first MMI. To keep the analysis simple, we still use ideal 3dB couplers. Instead we define E_{a2} and E_{b2} as the amplitude of the electric field at the input ports of the second MMI_2. Incorporating these terms, the interferometric matrix becomes [19],

$$\begin{bmatrix} M_{Interferometer} \end{bmatrix} = \begin{bmatrix} E_{a2}e^{j\beta\Delta L} & 0 \\ 0 & E_{b2} \end{bmatrix} \tag{3.7}$$

Assuming light is coupled into input port 1 of figure 3.1a with $E_1 = e^{j\omega t}$, the expression for the output intensity at ports 3 and 4 is given by [19],

$$\begin{bmatrix} I_{out}(3) \\ I_{out}(4) \end{bmatrix} = \frac{1}{4} \begin{bmatrix} E_{a2}^2/2 + E_{b2}^2/2 - E_{a2}E_{b2}\cos\beta\Delta L \\ E_{a2}^2/2 + E_{b2}^2/2 + E_{a2}E_{b2}\cos\beta\Delta L \end{bmatrix} \tag{3.8}$$

Ignoring loss and asymmetric splitting ratios, the normalized optical output power for the bar and cross ports of the AMZI is given by the following equations respectively [22],

$$I_{bar} = \sin^2\frac{\beta\Delta L}{2} \tag{3.9}$$

$$I_{cross} = \cos^2\frac{\beta\Delta L}{2} \tag{3.10}$$

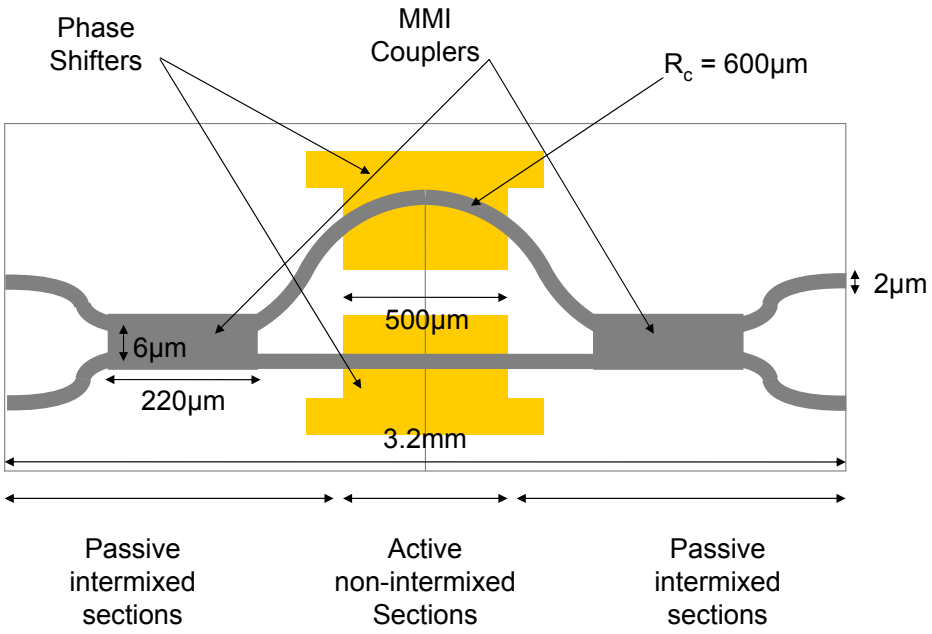

Figure 3.3: Detailed layout of the monolithically integrated AMZI

The channel spacing of the device is defined as the wavelength difference between two consecutive intensity maxima or minima in the bar and cross channels. Using equations (3.9) and (3.10), an expression for the channel spacing can be derived [22],

$$\Delta\lambda = \lambda_2 - \lambda_1 = \frac{\lambda_2\lambda_1}{2n_{eff}\Delta L} \tag{3.11}$$

3.3 Device Design

A schematic of the AMZI used in these experiments is shown in figure 3.3. It contains two 6 μm by 220 μm 3 dB MMI couplers and a 500 μm long phase shifter in each interferometer arm. The lower interferometer arm is a straight waveguide. The upper interferometer arm is a curved waveguide that has a radius of curvature of 600 μm. The total path length difference between the two arms is 455 μm. 2 μm ridge waveguides were used in the device. The device has a total length of 3.2 mm [18].

As was derived in the previous section, equations (3.9) and (3.10) govern the output

optical intensity of the AMZI. The channel spacing of the device was also expressed by equation (3.11) in the previous section. If the wavelength spacing between two channels is much less than the wavelength of the channels themselves, this equation simplifies to

$$\text{for } \Delta\lambda \ll \lambda_1, \lambda_2 \qquad \Delta\lambda = \frac{\lambda^2}{2n_{eff}\Delta L} \tag{3.12}$$

A channel spacing of 100G Hz (0.8 nm) was chosen for the AMZI to meet with the standard set by the International Telecommunication Union (ITU) for Dense Wavelength Division Multiplexing (DWDM) networks [19]. In the design of the AMZIs characterized here, an effective refractive index of 3.3 and an operating wavelength of 1550 nm was chosen [19]. Using equation (3.12), a path length difference of 455 μm would be necessary, in order to achieve the 0.8nm wavelength spacing.

Tuning of the peak wavelength is also possible by changing the optical path length difference $n_{eff}\Delta$L. This can be achieved by injecting current into the interferometer arms leading to a carrier induced refractive index change [20].

3.4 Device Fabrication

The fabrication process used for the AMZIs is the same as was described in [18]. The material structure was an InGaAs/InAlGaAs MQW heterostructure. It was grown by Metal Organic Chemical Vapour Deposition (MOCVD). The layers were lattice matched to a Si-doped InP wafer. A schematic of the layer structure is given in figure 3.4. The core is composed of 6, 7 nm InGaAs wells surrounded by 7, 8 nm $Al_{0.2}Ga_{0.27}In_{0.53}As$ barriers. The core is surrounded by an 80 nm thick GRIN $Al_xGa_yIn_{0.53}As$ layer, where x varies between 0.2 and 0.4. This is in turn surrounded by a 50 nm thick InAlAs layer. The use of the InAlAs and GRIN layers improve carrier and optical confinement and increase the carrier injection efficiency [18]. The top two layers of the device are a Zn doped 1400 nm InP upper cladding and a 200 nm InGaAs contact layer.

200nm	Contact Layer	**InGaAs**	
1400nm	Upper Cladding	**InP**	Zn doped
50nm		**InAlAs**	undoped
80nm	GRIN	**$Al_xGa_yIn_{0.53}As$**	undoped
8nm	Barrier	**$Al_{0.2}Ga_{0.27}In_{0.53}As$**	undoped
7nm	Well	**InGaAs**	undoped
8nm	Barrier	**$Al_{0.2}Ga_{0.27}In_{0.53}As$**	undoped
7nm	Well	**InGaAs**	undoped
8nm	Barrier	**$Al_{0.2}Ga_{0.27}In_{0.53}As$**	undoped
7nm	Well	**InGaAs**	undoped
8nm	Barrier	**$Al_{0.2}Ga_{0.27}In_{0.53}As$**	undoped
7nm	Well	**InGaAs**	undoped
8nm	Barrier	**$Al_{0.2}Ga_{0.27}In_{0.53}As$**	undoped
7nm	Well	**InGaAs**	undoped
8nm	Barrier	**$Al_{0.2}Ga_{0.27}In_{0.53}As$**	undoped
7nm	Well	**InGaAs**	undoped
8nm	Barrier	**$Al_{0.2}Ga_{0.27}In_{0.53}As$**	undoped
80nm	GRIN	**$Al_xGa_yIn_{0.53}As$**	undoped
50nm		**InAlAs**	undoped
	Substrate	**InP**	Si doped

Figure 3.4: Layer structure of the AMZI prior to intermixing

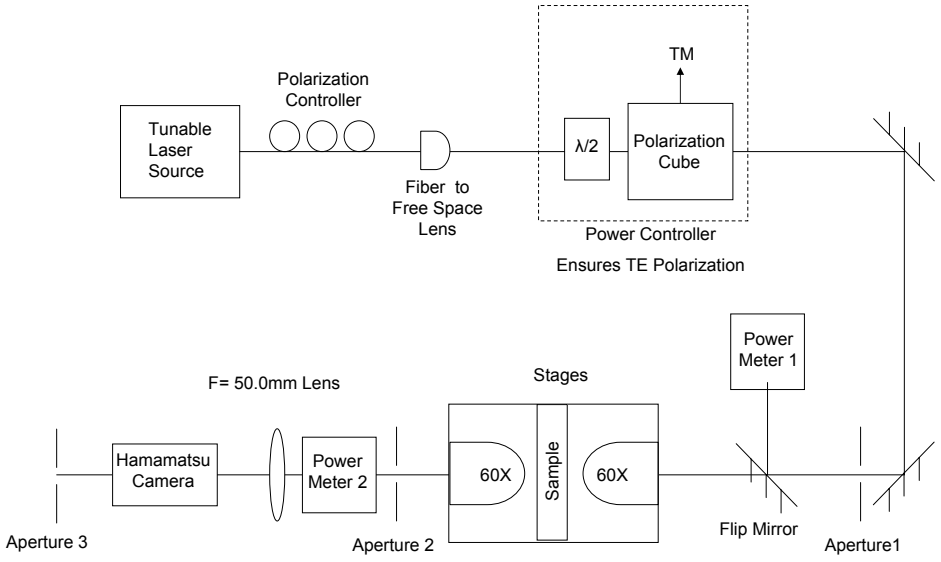

Figure 3.5: Free space setup used to characterize AMZI samples

The passive sections of the device were blue shifted by 110nm using QWI. The QWI technique used was the same sputtered SiO_2 technique described in Chapter 1 and in [11]. The phase shifter sections were not intermixed to preserve the electro-optic effect. They were protected during the intermixing process by a PECVD dielectric layer of SiO_2. The waveguides were defined by a CH_4H_2 reactive ion etch. Contact windows above the phase shifters were opened by a CHF_3 dry etch. This was finally followed with a 60s rapid thermal anneal at 360°C [32].

3.5 Results and Discussion

Characterization of the AMZI was carried out using the free space optics set up shown in figure 3.5. The Tunable Laser Source (TLS) used was a JDS Uniphase SWS15101, which can be tuned from 1480 nm to 1590 nm. Both TE and TM polarized light were injected into an input channel of the AMZI using a 60x objective lens. The output signal from the bar waveguide channel was recorded using another 60x objective lens and an Optical Power Meter (Newport 1830-C Optical Power Meter).

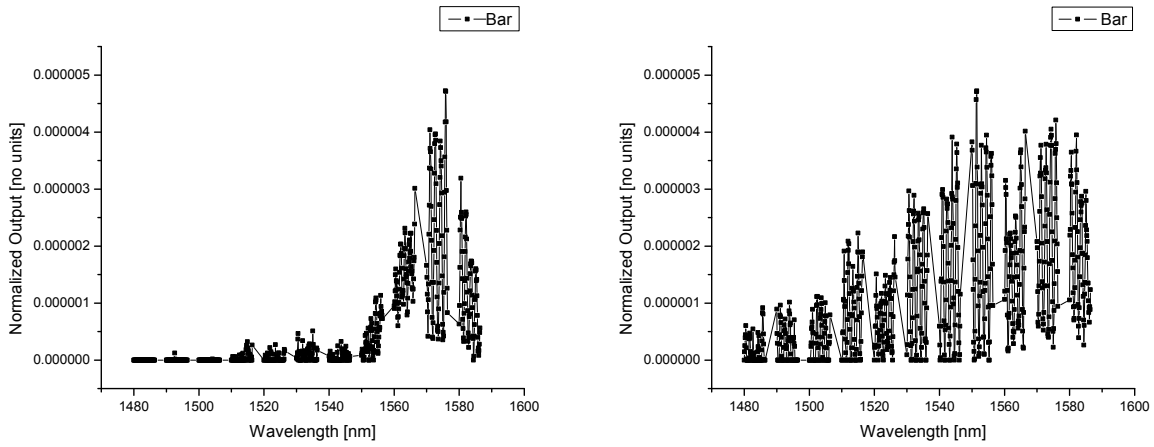

(a) (b)

Figure 3.6: Broad spectrum transmission measurements of the AMZI. (a) TE input light (b) TM input light

3.5.1 Transmission Spectrum

Figures 3.6a and b show the normalized transmission measurements over the entire spectrum of the TLS for TE and TM light respectively. The absorption bandedge for TE light is now around 1560 nm after intermixing. For TM light we were unable to see the output power decay to zero, as the cutoff wavelength for the TLS was 1480 nm however, the bandedge seems to be around 1510 nm. In order for the AMZI to achieve a high extinction ratio, a low imaginary part of the refractive index $\Delta\alpha$ and a high real part of the refractive index Δn are required [18]. This minimizes the power imbalance in each arm and ensures a strong phase shift. This can be achieved by operating the device far enough from the bandgap to minimize $\Delta\alpha$ but not so far as to lose phase shift capability. From figure 3.6 it appears that the optimal operating wavelength is between 1570 nm and 1580 nm.

Figure 3.7 shows the normalized output power of the bar port of the AMZI for both TE and TM polarizations. A channel spacing of 0.8 nm is observed in both the TE and

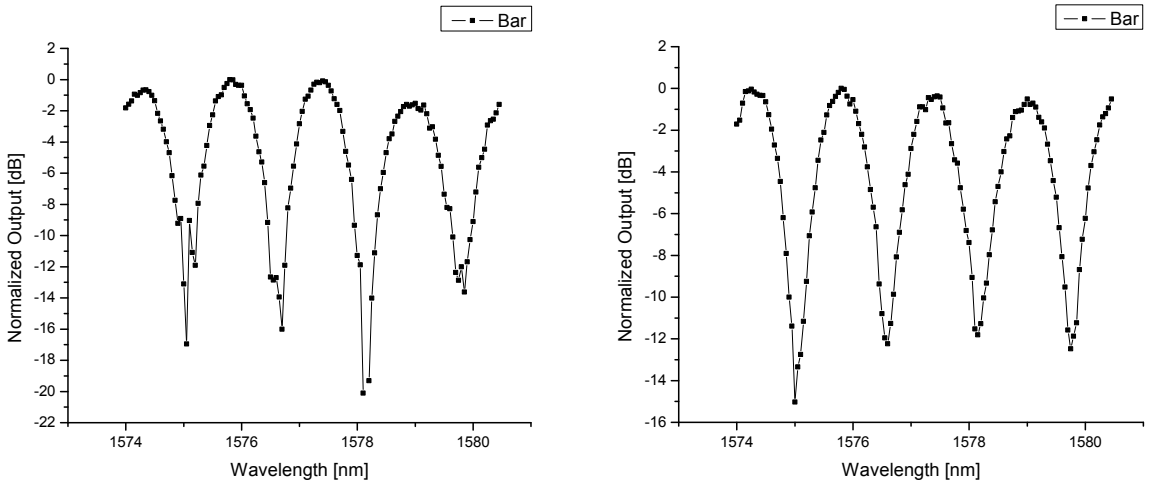

(a) (b)

Figure 3.7: Normalized output power for the bar port of the AMZI (a) TE input light (b) TM input light

TM transmission measurements as was expected. However the extinction ratio of the TE measurement was around 16 dB versus only 14 dB in the TM measurement. The polarization dependence of the AMZI is approximately 2 dB with a peak shift of about 0.03 nm between the TE and TM mode.

3.5.2 Device Tunability

As was stated previously, tuning of the device allows for the proper matching of the system wavelength. Tuning of the AMZI was achieved by injecting current into the longer interferometer arm. The injected carriers change the carrier concentration in the active region of the device, which in turn changes the absorption or the imaginary part of the refractive index $\Delta\alpha$. The real and imaginary parts of the refractive index are related by the Kramers-Kronig integral, which is how the carrier induced refractive index change takes place. The refractive index change leads to a phase change in the light travelling through the upper arm of the device. This phase difference between the upper and lower

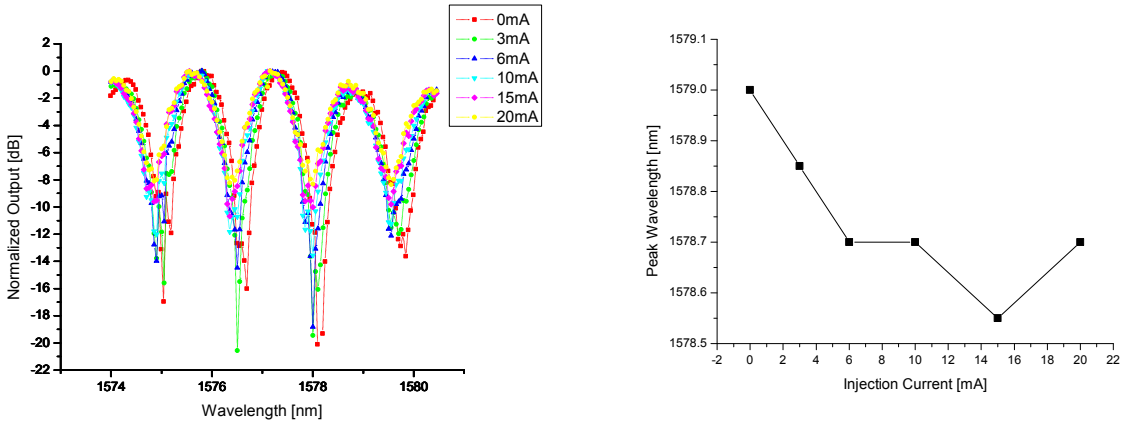

(a) (b)

Figure 3.8: Normalized output power for the bar port of the AMZI for various injected currents. (a) TE input light. (b) Corresponding peak shifts for TE input light

paths changes the interference conditions at the second MMI and results in a shifted transmission spectrum.

Figure 3.8a shows the normalized bar output of the AMZI with different amounts of current applied to the phase shifter for TE polarized light. Figure 3.8b illustrates the peak wavelength shift that was observed at each value of the injected current. A maximum shift of 0.45 nm was observed at a current value of 15 mA. Figure 3.8c and 3.8d illustrate the corresponding results for TM polarized light. For this polarization a maximum peakshift of 0.25 nm was observed at a current value of 15 mA.

Reducing the power imbalance in each arm by pre-biasing the interferometer arms would likely lead to an enhancement of the AMZI extinction ratio as was observed by Wong et al. [18]. However damaged waveguides due to fiber probing led to a very low coupling efficiency, making further experiments with these devices extremely difficult.

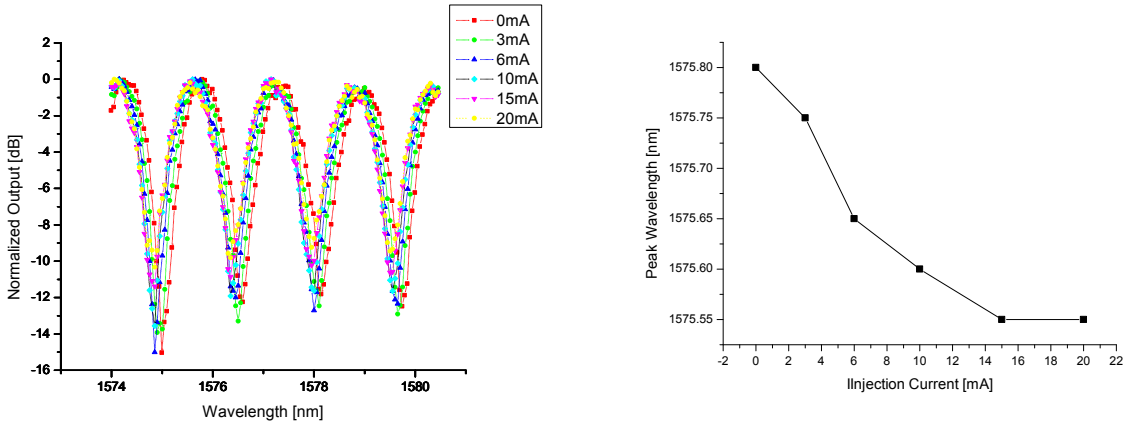

(c) (d)

Figure 3.8: (cont'd) Normalized output power for the bar port of the AMZI for various injected currents. (c) TM input light. (d) Corresponding peak shifts for TM input light

3.6 Conclusion

A monolithically integrated AMZI fabricated using a sputtered SiO_2 QWI technique was demonstrated. The device functions as a wavelength mux/demux with a channel spacing of 100 GHz (0.8 nm). Wavelength tuning was achieved through current injection into the active SOAs of the device. A maximum shift of 0.45 nm at an injection current of 15mA was observed. An extinction ratio as high as 16 dB was also achieved.

Chapter 4

Optical Logic

4.1 Introduction

All optical signal processing using non linear optics is critical to the progression of optical communications. Originally these devices required high powered pulsed lasers. With the advances made in semiconductor optical amplifiers, photonic crystal media and highly nonlinear fibers, nonlinear optical signal processing can now be achieved at lower powers [33]. Recently, interest in all optical signal processing has increased, with research being focused in the areas of, ultrafast switching, wavelength conversion, optical regeneration, optical tunable delays and SOA-based processing [34–41]. SOAs in particular have the advantage of a small footprint due to easy optical integration as well as low power consumption due to large optical nonlinearities with optical gain [38, 39].

In order for these devices to be more useful in future photonic networks, more complex functionality will be required of them. Previously Poustie et al. demonstrated the function of all optical regenerative memory, as well as another important function in Digital Optical Logic (DOL), the ability to perform modulo two addition of two binary data sequences with an all optical half adder [42, 43]. Their design of the half adder used 3 Terahertz Optical Asymmetric Demultiplexers (TOADs) as the optical switching

gates, and generated two outputs for the SUM and CARRY bits. The TOADs however, were not in integrated form.

In order for QWI to be considered as a viable integration technique, devices will have to demonstrate increased functionality, and cascadability. In this chapter we have chosen to outline how a Symmetric Mach-Zehnder Interferometer with asymmetrically placed SOAs may be used as the fundamental switching element in the design of a binary half adder. The first section outlines how a the symmetric MZI can be used to achieve the same functionality as a TOAD [44]. The second section demonstrates how such a device would function in a half adder. The design of the half adder is based on that which was first demonstrated by Poustie et al [43].

4.2 Symmetric MZI Device Functionality

In Optical Time Division Multiplexing (OTDM) systems, many users multiplex their data onto an optical fiber. Each user has a time slot of T_{bit} seconds within a time frame of T_{frame} seconds. In order for a receiver to demultiplex a particular data stream he has to be able to sample the correct time slot within each frame [44]. These requirements can be met with a Symmetric Mach-Zehnder Interferometer (SMZI) with asymmetrically placed SOA's that have a rise time τ_{rise} and τ_{fall} time which satisfy equation (4.1) [44].

$$\tau_{rise} < T_{bit} \ll \tau_{fall} < T_{frame} \tag{4.1}$$

Nonlinearities in SOAs generally have a strong response and slow recovery [44]. A strong control signal can be used to saturate the gain of an SOA and thereby modulate the phase of any signals propagating through the SOA before it recovers. This is known as Cross Phase Modulation (XPM) [45]. Although the gain saturation has a fast turn on time τ_{rise} it's fall time τ_{fall} is limited by the relatively slow carrier recovery time within the SOA which can be orders of magnitude larger. The nonlinearity is therefore capable

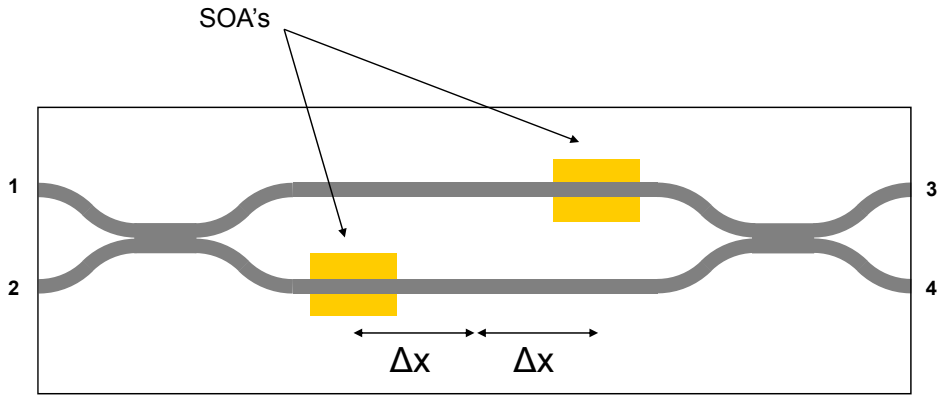

Figure 4.1: Schematic Layout of the Symmetric Mach Zehnder Interferometer

of satisfying equation (4.1).

The symmetric MZI works in the same fashion as the AMZI described in Chapter 3. Light entering input port 1 is split into either arm by the first 2x2 3 dB MMI. After returning to the second MMI the two fields interfere so that all the light exits from the cross port. If the field in one arm experiences a different optical path length due to a change in the refractive index, the emerging light can be made to exit from the bar port.

The symmetric MZI described here has SOAs in either arm which are offset from the centre of the MZI by a distance Δx, figure 4.1.

Signal pulses entering through input port 1 are split into the upper and lower arm of the interferometer and will be referred to as UPPER and LOWER respectively. They pass through their respective SOAs once. If a control pulse is injected into one of the output ports, it too is split and passes through each SOA once as it propagates through the MZI in the opposite direction to the signal. The control pulse can saturate the gain of the SOAs, whereas the signal does not have enough power. The optical properties of the SOA undergo a quick transition and then the gain slowly recovers.

In order to understand how the MZI is used as a demultiplexing switch we explain three scenarios. First, a signal pulse enters input port 2 of the MZI. It is split into an UPPER and LOWER signal. A control pulse also enters the output of the MZI. As

the control traverses the SOAs, gain saturation occurs causing a transition in its optical properties. If the signal pulse enters the MZI much earlier than the control, both the UPPER and LOWER signal have traversed their respective SOAs when the transition happens. Since no change in the optical properties is experienced by either pulse, they interfere in the normal manner and exit from the cross port of the MZI. This is illustrated in figure 4.2 where the UPPER and LOWER pulses are labeled 'A' and are unshaded to signify the fact that they experience pre-transition properties of the SOAs.

Next we examine what happens when the signal pulse enters the MZI much after the control pulse, such that both the UPPER and LOWER signals enter their respective SOAs after the transition has occurred. Both pulses are labeled 'C' in figure 4.2 and are shaded to reflect the fact that they experience the post-transition properties of the SOAs. The UPPER signal pulse travels $2\Delta x$ further than the lower pulse to get to its SOA. As a result it gets to the the SOA $2\Delta x/v$ seconds later, where v is the speed of light in the material. The optical properties of the SOAs experienced by the UPPER and LOWER pulse will be the same, if the SOAs fall time satisfies the inequality (4.2) [44],

$$\tau_{fall} \gg 2\Delta x/v \tag{4.2}$$

Once again the phase of the two pulses is the same at the second MMI and they interfere constructively and emerge from the cross port.

Finally we look at case 'B' in figure 4.2. Here the signal pulse enters the MZI at approximately the same time as the control pulse. Now the LOWER pulse has passed its SOA when the transition occurs however, the UPPER pulse has not. The UPPER pulse is shaded to reflect that it experiences post-transition properties of the SOA whereas the LOWER pulse is not. As a result destructive interference between the two pulses occurs at the second MMI and the pulse now emerges from the bar port.

The transition in the optical properties of the SOA creates a switching window for the

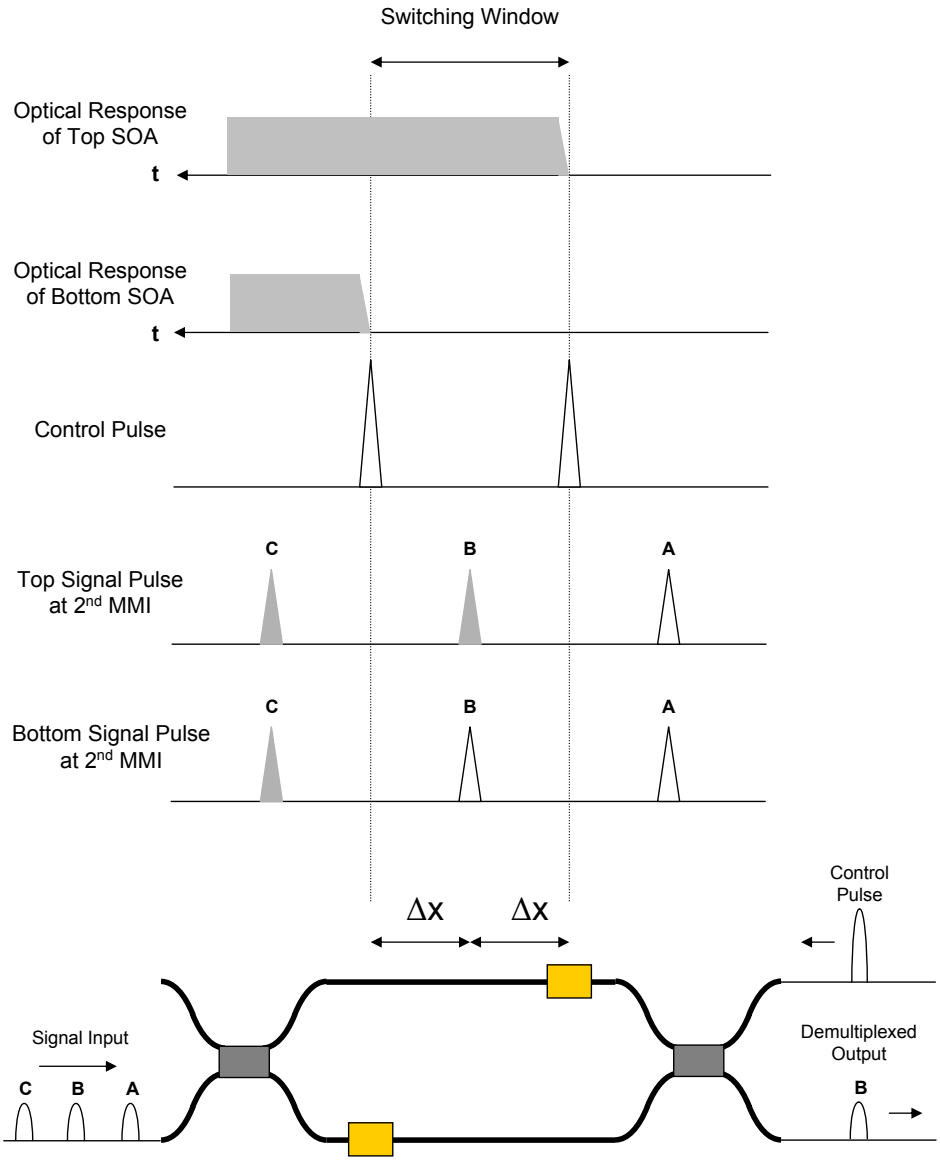

Figure 4.2: Illustration of the operation of the SMZI switch.

MZI. Pulses that exit from the MZI bar port are less than Δx from the MZI centre when the gain saturation in the first SOA occurs. The resulting switching window is therefore $2\Delta x/v$ seconds long. In order to demultiplex any bit from the data stream, $2\Delta x/v$ must be less than the bit period T_{bit}. A second bit can not be demultiplexed until the SOA gain has returned to normal. As a result the frame period T_{frame} should be greater than the fall time of the SOA, τ_{fall}. As such, equation (4.1) is established [44].

The length of the sampling window has both upper and lower limits. The upper limit is set by the gain recovery time of the SOA as was established in equation (4.1). However, we are more interested in the lower limits on the sampling window. The fundamental limits are set by the rise time of the SOA and the propagation time through the SOA. The greater of these sets a lower limit on the switching window [44]. The rise time of the SOA is generally less than 1 ps, however the propagation delay of a 500 μm SOA is around 5.5 ps. This can be reduced by reducing the SOA size. However if we use 5.5 ps with a refractive index of 3.3 (as was used in the design of the AMZIs) this leads to a Δx of 250 μm and a separation distance of 500 μm between the SOAs. This is a reasonable distance for an integrated device and works out to be slightly larger than the path length difference that was used in the AMZI.

4.3 All Optical Binary Half Adder

Our all optical design uses 2 Symmetric MZI's which were described in the previous section, to perform the half adder function. It has two outputs, one for the SUM bits and the other for the CARRY bits. The design is based on a half adder design by Poustie et al. in which TOADs were utilized as switching gates [43].

Electronic gate symbols are used in figure 4.3 to create the electronic logic diagram of the serial half adder.

The layout for the all optical realization of this circuit is shown in figure 4.4.

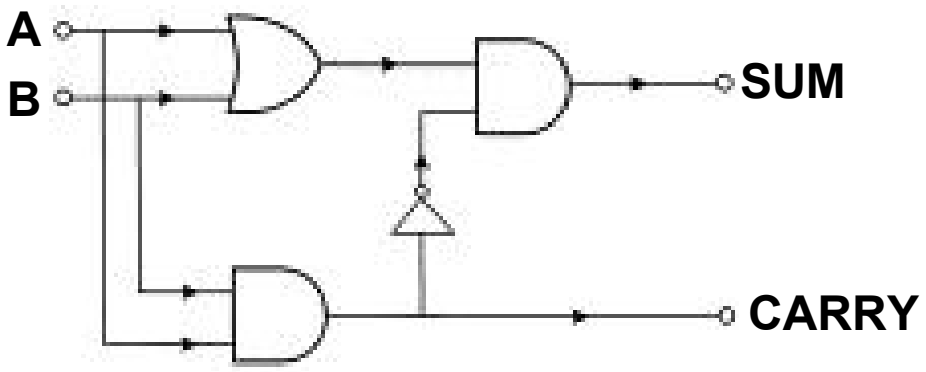

Figure 4.3: Electronic logic diagram for a binary half adder

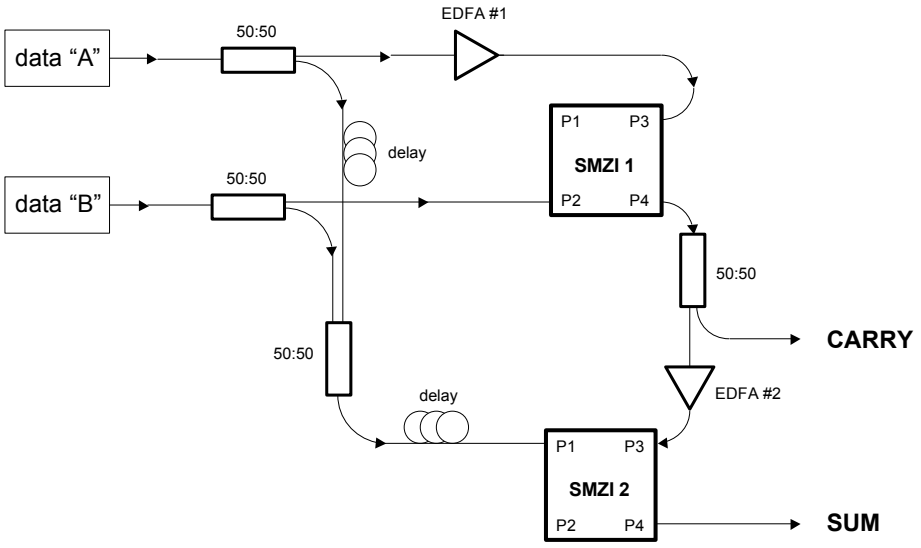

Figure 4.4: Schematic layout for the implementation of an all optical binary half adder

Each SMZI is represented as a block with two inputs and two outputs that are used in the same manner as was demonstrated previously. Adjustable optical delay lines would be required to synchronize the pulses in order for the correct switching operations to take place in the SMZIs. Control pulses could be obtained using Erbium Doped Fibre Amplifiers (EDFAs) to amplify the signal pulses.

A 50:50 couplers to split the A and B signals to the 2 SMZIs. The AND operation of signals A and B is produced by SMZI1. It is biased such that light entering generally exits the cross port. However, in the instance where both A and B are a logic ONE, signal A is used as a control to switch the output to the bar port thereby generating the CARRY bit of the operation. In all other cases a logic ZERO is the result and no light exits the bar port. The CARRY bit is then amplified and used as a control signal for SMZI2. In the paper by Poustie et al. this last step requires the CARRY bit to be wavelength converted using a 3rd TOAD or have a shift in polarization in order to be distinguished from the signal pulses [43]. Since the control pulse of the MZI is propagating in the opposite direction of the input pulses, this is unnecessary. A 50:50 coupler is used to create the logic OR of the inputs A and B. The correct bit-serial synchronization is maintained by delaying one signal relative to the other in order to account for path length differences. The output of the OR is also delayed (in order to account for path length differences of the pulse traveling through SMZI1) and then fed into the input of SMZI2. SMZI2 inverts the CARRY bit and provides the last AND gate in the logic diagram, figure 4.3. The cross port of SMZI2 is used as the primary output. SMZI2 is biased such that all light exits the cross port in the absence of a control pulse. As a result, if A=1 and B=0 or if A=0 and B=1 then the output is a logic ONE. However if A and B = 1, then the output of SMZI1 is used to switch SMZI2 such that light exits the bar port, in which case a logic ZERO exits the cross port. The modulo-2 addition of signals A and B is completed, with both SUM and CARRY outputs.

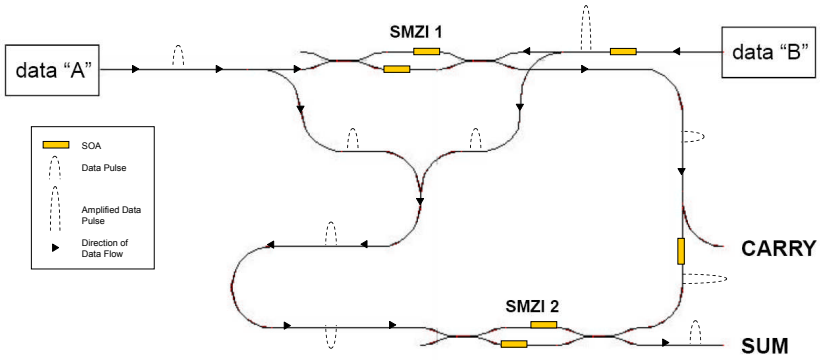

Figure 4.5: Schematic layout for the implementation of a monolithically integrated all optical binary half adder

4.3.1 Integrated Binary Half Adder

The previously described All Optical Half Adder also has the potential to be fully monolithically integrated. Although this stage is quite complicated and would require further development of the integration methods, we present some considerations for integrating such a device.

Figure 4.5 is a schematic of an integrated all optical half adder. In the design of this circuit 2 μm ridge waveguides were used throughout the device. The 50:50 couplers in the previous layout have been replaced with MMI couplers. Each coupler is 6x196 μm. In the previous chapter this was found to be the optimum length for couplers in the new layer structure. From the simulations in Chapter 2, a 600 μm bend radius was used for all bends to minimize loss. The EDFAs used to regenerate the signal in the previous layout are replaced here with SOAs. Lastly because optical delays are not so easy to integrate in a device, the waveguides have been designed with the correct path lengths. This is to ensure that both signals arrive with the correct bit serial synchronization. This is also the reason that the signal inputs have been placed on opposite sides of the chip.

Integration issues do arise which would need to be dealt with in the design of a final device. For example a tunable delay may be required in order to optimize functionality.

This could be achieved using a heated waveguide as was done by Lai et al. [22]. Providing the correct path lengths however, would limit the tuning range necessary. Secondly, optical isolators may be required in order to prevent light from re-entering the laser cavities on the opposite sides of the chip. Although there has not been much research on monlithically integrated isolators, future developments may make this a viable option.

In order for the Mach-Zehnder Interferometer switches to function well in a cascaded configuration like this, they also need to meet certain requirements. Gavioli et al. determined that for SOA-based switches to achieve cascadability both noise suppression and extinction ratio enhancement are required [46]. They also reasoned that XPM based SOA switches were better suited for this task than Cross Gain Modulation (XGM) ones. Although the Symmetric MZI we presented previously is XPM based, further characterization of the device would be required to determine how well it accomplishes these requirements. Hinton et al. also determined that an extinction ratio greater than 10 dB would be required in order to maintain signal quality in a cascaded device [41]. As was shown in Chapter 3 the AMZI is capable of this and we could expect the same behavior from Symmetric MZI's as well.

4.4 Conclusion

The Symmetric Mach-Zehnder Interferometers functionality as a demultiplexer for OTDM systems was described. It uses the strong slow gain saturation of the SOAs to open a switching window, during which pulses are demultiplexed from the data stream. The control and signal pulses do not need to be distinguished in wavelength as the propagate in opposite directions and enter and exit through different ports. The possibility of such devices being used to create an optical binary half adder was also described. The layout for such a circuit as well as its potential for full monolithic integration were presented.

Chapter 5

Conclusion

In conclusion this thesis reported on the simulation, characterization and development of monolithically integrated devices. These devices were fabricated using a QWI sputtered SiO_2 technique, which is a flexible, reliable and cost effective approach to integration.

First Lumerical's MODE Solutions software was used to simulate the active MQW layer structure as well as an approximation to the intermixed structure of the devices. No significant differences between the active and passive sections of the devices were observed. Simulations of the AMZI layer structure and a newly developed layer structure provided information on the supported modes, effective refractive indices and optimum physical dimensions of the structures. A ridge width of 1.5 μm and a bend radius above 600 μm was shown to minimize loss in both structures. Such information can be used by our collaborators in Glasgow to optimize future devices and layer designs.

Characterization of an AMZI fabricated using the sputtered SiO_2 technique was also carried out. The device was shown to have a channel spacing of 100 GHz (0.8 nm) with an extinction ratio as high as 16 dB. Tuning of the device was achieved through current injection into the active SOAs. A maximum peak shift of 0.45 nm was achieved at a current value of 15 mA. These characteristics were consistent with the design of the device and demonstrated the capacity of this QWI technique to produce monolithically

integrated devices.

Finally the design and operating principle of an integrated All Optical Binary Half Adder were presented. Such a device demonstrates the potential for optical circuits with increased functionality to be fabricated using monolithic integration techniques.

5.1 Future Work

The work in this thesis has laid the foundation for the development of optimized monolithically integrated devices. Currently MODE Solutions software has been used to simulate different layer structures using only refractive index values obtained from the literature. Experimentally determining these values as well as the effect strain and doping have on their optical properties of the layers would lead to more accurate modeling.

Presently our collaborators in Glasgow are also working on producing a set of waveguides with various amounts of intermixing. Characterization of such a sample would allow us to better determine the effect intermixing has on the optical properties of the device. This would also allow us to develop more optimized monolithically integrated devices. Pump probe measurements on active SOAs would help determine their dynamics, and whether or not the SMZI structure would function well as a demultiplexing switch.

Lastly with the information obtained from these characterization experiments, an attempt at fabricating a more complex circuit as was proposed in Chapter 4 could be made. This would be a major development in monolithic integration, and would be a practical next step to such experiments.

Appendix A

Layer Structure Details

Layer	Material	Repeat	Mole Fraction (x)	Mole Fraction (y)	Thickness(um)	Dopant	Type	Refractive Index
27	In(x)Ga(1-x)As	1	0.53		0.2	Zn	P	3.6455
26	InP	1			1.4	Zn	P	3.16697
25	Al(x)In(1-x)As	1	0.48		0.05	Undoped		3.2
24	Al(x)Ga(y)In(1-x-y)As	1	0.4	0.07	0.02	Undoped		3.291
23	Al(x)Ga(y)In(1-x-y)As	1	0.3	0.17	0.02	Undoped		3.351
22	Al(x)Ga(y)In(1-x-y)As	1	0.25	0.22	0.02	Undoped		3.382
21	Al(x)Ga(y)In(1-x-y)As	1	0.2	0.27	0.02	Undoped		3.416
QB	Al(x)Ga(y)In(1-x-y)As	6	0.2	0.27	0.008	Undoped		3.416
QW	In(x)Ga(1-x)As	6	0.53		0.007	Undoped		3.6455
QB	Al(x)Ga(y)In(1-x-y)As	1	0.2	0.27	0.008	Undoped		3.416
6	Al(x)Ga(y)In(1-x-y)As	1	0.2	0.27	0.02	Undoped		3.416
5	Al(x)Ga(y)In(1-x-y)As	1	0.25	0.22	0.02	Undoped		3.382
4	Al(x)Ga(y)In(1-x-y)As	1	0.3	0.17	0.02	Undoped		3.351
3	Al(x)Ga(y)In(1-x-y)As	1	0.4	0.7	0.02	Undoped		3.291
2	Al(x)In(1-x)As	1	0.48		0.05	Undoped		3.2
1	InP	1			1.4	Si	N	3.16697
Substrate	InP	1				Si	N	3.16697

Figure A.1: AMZI Layer Structure Details

Layer	Material	Repeat	Mole Fraction (x)	Mole Fraction (y)	Thickness(um)	Dopant	Type	Refractive Index
24	In(x)Ga(1-x)As	1	0.53		0.2	Zn	P	3.6455
23	In(x)Ga(1-x)As(y)P(1-y)	1	0.71	0.62	0.05	Zn	P	3.47
22	InP	1			0.1	Zn	P	3.16697
21	InP	1			1.5	Zn	P	3.16697
20	In(x)Ga(1-x)As(y)P(1-y)	1	0.85	0.33	0.02	Zn	P	3.31
19	InP	1			0.05	Zn	P	3.16697
18	Al(x)Ga(y)In(1-x-y)As	1	0.423	0.047	0.06	Zn	P	3.2794
17	Al(x)Ga(y)In(1-x-y)As	1	0.3384 to 0.423	0.1316 to 0.047	0.06	Undoped		3.3277 to 3.2794
QB	Al(x)Ga(y)In(1-x-y)As	1	0.2244	0.2856	0.01	Undoped		3.3892
QW	Al(x)Ga(y)In(1-x-y)As	5	0.0696	0.2204	0.006	Undoped		3.5532
QB	Al(x)Ga(y)In(1-x-y)As	5	0.2244	0.2856	0.01	Undoped		3.3892
5	Al(x)Ga(y)In(1-x-y)As	1	0.423 to 0.3384	0.047 to 0.1316	0.06	Undoped		3.2794 to 3.3277
4	Al(x)Ga(y)In(1-x-y)As	1	0.423	0.047	0.06	Si	N	3.2794
3	Al(x)Ga(y)In(1-x-y)As	1	0.4042 to 0.423	0.0658 to 0.047	0.01	Si	N	3.2898 to 3.2794
2	InP	1			0.5	Si	N	3.16697
1	InP	1			0.3	Si	N	3.16697
Substrate	InP	1				Si	N	3.16697

Figure A.2: New Generation Layer Structure Details

Appendix B

MODE Scripts

B.1 Convergence Script

```
#Program:  Calculates and plots effective index and loss as a
#function of the actual number of mesh points for both a uniform and
#non-uniform mesh
#Author:  Roger D'Abreo
#Date:  April 1, 2008

#define a vector for the target number of mesh points
y_target=linspace(125,200,8);

#initialize actual number of mesh points variable
y_actual=y_target;

#initialize effective index matrix for uniform and non-uniform mesh
results mode_n=matrix(8,2);
```

```
#initialize loss variable matrix for uniform and non-uniform mesh
results mode_loss=matrix(8,2);

#loop for both the non-uniform and uniform mesh
for (j=1:2){
    #set the first guess index
    analysis;
    set("n",3.23);
    #loop for each number of mesh points
    for(i=1:length(y_target)){
        #if non-uniform
        if (j==1){
            #enable override regions
            switchtolayout;
            simulation;
            select("mesh");
            set("override y mesh",1);
            set("override x mesh",0);
            #set target number of mesh points
            select("MODE");
            set("mesh cells x",50);
            set("mesh cells y",y_target(i));
            #get actual number of mesh points, with non-uniform mesh
            mesh;
            simulation;
            select("MODE");
            y_actual(i)=get("actual mesh cells y");
```

```
#if uniform
}else{
    #disable override regions
    switchtolayout;
    simulation;
    select("mesh");
    set("override y mesh",0);
    set("override x mesh",0);
    #set number of mesh points
    select("MODE");
    set("mesh cells x",50);
    set("mesh cells y",y_actual(i));
}
#calculate modes
findmodes;
#finds new mode which overlaps best with reference mode
fund = bestoverlap("FUND");
#extract the neff and propagation loss for the correct mode
mode_n(i,j)=getdata(fund,"neff");
mode_loss(i,j)=getdata(fund,"loss");
#clear reference data
cleardcard;
#copy new mode as reference
copydcard(fund,"FUND");
#print current status to screen
?"current run=" + num2str(i) + " of 8      loss (dB/m)=" + num2str(mode_loss(
#save data to file
```

```
        savedata("mesh_convergence",y_target,y_actual,mode_n,mode_loss);
    }
}
#create final plots closeall;

plot(y_actual,mode_n,"number of y points","effective index");
legend("non-uniform","uniform");

plot(y_actual,mode_loss,"number of y points","loss (dB/m)");
legend("non-uniform","uniform");
```

B.2 Bend Radius Script

```
#Program:  Calculates and plots loss as a function of bend radius
#Author:  Roger D'Abreo
#Date:  April 1, 2008

#define a vector of radius of curvatures (ROCs) in SI units
rad=linspace(200e-6,1000e-6,17);

#reserve memory for measured loss at each ROC
fundloss=matrix(length(rad),1);

#switch to analysis tab
analysis;

#calculates the loss at each ROC
```

```
for(i=1:length(rad)) {
    #specify we want to analyze waveguide bends
    set("bent waveguide",1);
    #set bend radius
    set("bend radius",rad(i));
    #solve for the waveguide modes
    mesh;
    findmodes;
    #find the new mode which overlaps best with the reference mode
    fund = bestoverlap("FUND");
    #extract the propagation loss for the correct mode
    fundloss(i) = getdata(fund,"loss");
    #clear reference data
    cleardcard;
    #copy new mode as reference
    copydcard(fund,"FUND");
    #set effective index of current mode to guess for next mode
    new_guess_index = getdata(fund,"neff");
    set("n",new_guess_index);
    #print current status to screen
    ?"current run=" + num2str(i) + " of 17      loss (dB/m)=" + num2str(fundloss(i));
    #save the data to a file
    savedata("bend_radius",rad,fundloss);
}

#plot results
plot(rad*1e6,fundloss,"radius (um)","loss (dB/m)","");
```

B.3 Ridge Width Script

```
#Program:  Calculates and plots loss as a function of ridge width
#Author:  Roger D'Abreo
#Date:  April 1, 2008

#define a vector of ridge widths (RW) in SI units
width=linspace(0.5e-6,4e-6,15);

#reserve memory for measured loss at each RW
fundloss=matrix(length(width),1);

#calculates the loss at each RW
for(i=1:length(width)) {
    #set ridge width for the correct layers
    switchtolayout;
    structures;
    select("U_cladding");
    set("x span",width(i));
    select("contact");
    set("x span",width(i));
    #switch to analysis tab
    analysis;
    #solve for the waveguide modes
    mesh;
```

```
    findmodes;
    #find the new mode which overlaps best with the reference mode
    fund = bestoverlap("FUND");
    #extract the propagation loss for the correct mode
    fundloss(i) = getdata(fund,"loss");
    #clear reference data
    cleardcard;
    #copy new mode as reference
    copydcard(fund,"FUND");
    #set effective index of current mode to guess for next mode
    new_guess_index = getdata(fund,"neff");
    set("n",new_guess_index);
    #print current status to screen
    ?"current run=" + num2str(i) + " of 15      loss (dB/m)=" + num2str(fundloss(i));
    #save the data to a file
    savedata("ridge_width",width,fundloss);
}

#plot results

plot(width*1e6,fundloss,"ridge width (um)","loss (dB/m)","");
```

Bibliography

[1] E. H. Li, E. S. Koteles, and J. H. Marsh, "Introduction to the issue on interdiffused quantum-well materials and devices," *Ieee Journal of Selected Topics in Quantum Electronics*, vol. 4, no. 4, pp. 581–583, 1998, 124HY Times Cited:13 Cited References Count:0.

[2] E. J. Skogen, "Quantum well intermixing for wavelength-agile photonic integrated circuits," Ph.D. dissertation, University of California, 2003.

[3] S. Charbonneau, E. S. Koteles, P. J. Poole, J. J. He, G. C. Aers, J. Haysom, M. Buchanan, Y. Feng, A. Delage, F. Yang, M. Davies, R. D. Goldberg, P. G. Piva, and I. V. Mitchell, "Photonic integrated circuits fabricated using ion implantation," *Ieee Journal of Selected Topics in Quantum Electronics*, vol. 4, no. 4, pp. 772–793, 1998, 124HY Times Cited:47 Cited References Count:59.

[4] J. J. M. Binsma, P. J. A. Thijs, T. vanDongen, E. J. Jansen, A. A. M. Staring, G. N. vandenHoven, and L. F. Tiemeijer, "Characterization of butt-joint ingaasp waveguides and their application to 1310nm dbr-type mqw gain-clamped semiconductor optical amplifiers," *Ieice Transactions on Electronics*, vol. E80c, no. 5, pp. 675–681, 1997, xb291 Times Cited:9 Cited References Count:16.

[5] R. C. Alferness, U. Koren, L. L. Buhl, B. I. Miller, M. G. Young, T. L. Koch, G. Raybon, and C. A. Burrus, "Broadly tunable ingaasp/inp laser based on a vertical

coupler filter with 57-nm tuning range," *Applied Physics Letters*, vol. 60, no. 26, pp. 3209–3211, 1992, ja806 Times Cited:81 Cited References Count:10.

[6] M. Aoki, M. Suzuki, H. Sano, T. Kawano, T. Ido, T. Taniwatari, K. Uomi, and A. Takai, "Ingaas/ingaasp mqw electroabsorption modulator integrated with a dfb laser fabricated by band-gap energy control selective-area mocvd," *Ieee Journal of Quantum Electronics*, vol. 29, no. 6, pp. 2088–2096, 1993, lz008 Times Cited:78 Cited References Count:36.

[7] B. Mason, G. A. Fish, S. P. DenBaars, and L. A. Coldren, "Widely tunable sampled grating dbr laser with integrated electroabsorption modulator," *Ieee Photonics Technology Letters*, vol. 11, no. 6, pp. 638–640, 1999, 199CR Times Cited:42 Cited References Count:8.

[8] S. G. Ayling, J. Beauvais, and J. H. Marsh, "Spatial control of quantum-well intermixing in gaas aigaas using a one-step process," *Electronics Letters*, vol. 28, no. 24, pp. 2240–2241, 1992, ka244 Times Cited:21 Cited References Count:3.

[9] H. Jones-Bey, "Optical integrated circuits benefit from quantum-well intermixing," 2002.

[10] W. D. Laidig, N. Holonyak, M. D. Camras, K. Hess, J. J. Coleman, P. D. Dapkus, and J. Bardeen, "Disorder of an alas-gaas super-lattice by impurity diffusion," *Applied Physics Letters*, vol. 38, no. 10, pp. 776–778, 1981, lr637 Times Cited:427 Cited References Count:13.

[11] S. D. McDougall, O. P. Kowalski, C. J. Hamilton, F. Camacho, B. C. Qiu, M. L. Ke, R. M. De La Rue, A. C. Bryce, and J. H. Marsh, "Monolithic integration via a universal damage enhanced quantum-well intermixing technique," *Ieee Journal of Selected Topics in Quantum Electronics*, vol. 4, no. 4, pp. 636–646, 1998, 124HY Times Cited:32 Cited References Count:27.

[12] N. Holonyak, "Impurity-induced layer disordering of quantum-well heterostructures: Discovery and prospects," *Ieee Journal of Selected Topics in Quantum Electronics*, vol. 4, no. 4, pp. 584–594, 1998, 124HY Times Cited:13 Cited References Count:74.

[13] A. McKee, C. J. McLean, G. Lullo, A. C. Bryce, R. M. DelaRue, J. H. Marsh, and C. C. Button, "Monolithic integration in ingaas-ingaasp multiple-quantum-well structures using laser intermixing," *Ieee Journal of Quantum Electronics*, vol. 33, no. 1, pp. 45–55, 1997, wa194 Times Cited:41 Cited References Count:26.

[14] M. Guden and J. Piprek, "Material parameters of quaternary iii-v semiconductors for multilayer mirrors at 1.55 mu m wavelength," *Modelling and Simulation in Materials Science and Engineering*, vol. 4, no. 4, pp. 349–357, 1996, vq556 Times Cited:28 Cited References Count:26.

[15] Y. Suzuki, H. Iwamura, T. Miyazawa, A. Wakatsuki, and O. Mikami, "Polarization-dependent refractive-index change induced by superlattice disordering," *Ieee Journal of Quantum Electronics*, vol. 32, no. 11, pp. 1922–1931, 1996, vp675 Times Cited:5 Cited References Count:24.

[16] T. C. Kleckner, "Quasi-phase-matched nonlinear frequency conversion in periodically disordered gaas/alas superlattice-core waveguides," Ph.D. dissertation, University of Glasgow, 2002.

[17] F. Ladouceur and J. D. Love, *Silica-based buried channel waveguides and devices*, 1st ed., ser. Optical and quantum electronics series ; 3. London ; New York: Chapman and Hall, 1996, franocois and John D. Love ill. ; 24 cm.

[18] H. Y. Wong, W. K. Tan, A. C. Bryce, J. H. Marsh, J. M. Arnold, A. Krysa, and M. Sorel, "Current injection tunable monolithically integrated engaas-inalgaas asymmetric mach-zehnder interferometer using quantum-well intermixing," *Ieee Photon-*

ics Technology Letters, vol. 17, no. 8, pp. 1677–1679, 2005, 949OX Times Cited:0 Cited References Count:13.

[19] H. Y. Wong, "Ingaas/ina1gaas monolithically integrated mach-zehnder interferometer devices," Ph.D. dissertation, University of Glasgow, 2005.

[20] S. Matsuo, Y. Yoshikuni, T. Segawa, Y. Ohiso, and H. Okamoto, "A widely tunable optical filter using ladder-type structure," *Ieee Photonics Technology Letters*, vol. 15, no. 8, pp. 1114–1116, 2003, 704YX Times Cited:3 Cited References Count:6.

[21] R. Hoshi, K. Nakatsuhara, and T. Nakagami, "Optical switching characteristics in si-waveguide asymmetric mach-zehnder interferometer having ferro-electric liquid crystal cladding," *Electronics Letters*, vol. 42, no. 11, pp. 635–636, 2006, 063PN Times Cited:2 Cited References Count:4.

[22] Q. Lai, M. Lanker, W. Hunziker, and H. Melchior, "Tunable wavelength-selection switch and multiplexer/demultiplexer based on asymmetric silica-on-silicon mach-zehnder interferometer," *Electronics Letters*, vol. 34, no. 3, pp. 266–267, 1998, yy494 Times Cited:8 Cited References Count:4.

[23] D. W. Kim, A. Barkai, R. Jones, N. Elek, H. Nguyen, and A. S. Liu, "Silicon-on-insulator eight-channel optical mulltiplexer based on a cascade of asymmetric mach-zehnder interferometers," *Optics Letters*, vol. 33, no. 5, pp. 530–532, 2008, 282KE Times Cited:0 Cited References Count:9.

[24] H. M. Kim, D. C. Kim, J. S. Kim, J. H. Kim, K. E. Pyun, S. G. Kang, H. R. Choo, and K. H. Yoo, "Design and fabrication of an 8-channel inp arrayed waveguide grating demultiplexer module with wide tuning range," *Journal of the Korean Physical Society*, vol. 38, no. 3, pp. 173–176, 2001, 411MA Times Cited:2 Cited References Count:12.

[25] P. V. Studenkov, M. R. Gokhale, J. Wei, W. Lin, I. Glesk, P. R. Prucnal, and S. R. Forrest, "Monolithic integration of an all-optical mach-zehnder demultiplexer using an asymmetric twin-waveguide structure," *Ieee Photonics Technology Letters*, vol. 13, no. 6, pp. 600–602, 2001, 434UB Times Cited:15 Cited References Count:9.

[26] E. Jahn, N. Agrawal, H. J. Ehrke, R. Ludwig, W. Pieper, and H. G. Weber, "Monolithically integrated asymmetric mach-zehnder interferometer as a 20gbit/s all-optical add/drop multiplexer for otdm systems," *Electronics Letters*, vol. 32, no. 3, pp. 216–217, 1996, ul768 Times Cited:16 Cited References Count:9.

[27] F. Ratovelomanana, N. Vodjdani, A. Enard, G. Glastre, D. Rondi, R. Blondeau, C. Joergensen, T. Durhuus, B. Mikkelsen, K. E. Stubkjaer, A. Jourdan, and G. Soulage, "An all-optical wavelength-converter with semiconductor optical amplifiers monolithically integrated in an asymmetric passive mach-zehnder interferometer," *Ieee Photonics Technology Letters*, vol. 7, no. 9, pp. 992–994, 1995, rv016 Times Cited:26 Cited References Count:7.

[28] R. Paschotta, "Encyclopedia of laser physics and technology," 2008.

[29] S. Cao, L. Sun, J. Noad, R. James, D. Coulas, G. Lovell, E. Higgins, and K. Laliberte, "Multimode interference couplers for 2x2 high speed gaas-gaalas electro-optic switches," p. 61160O, 2006.

[30] L. B. Soldano and E. C. M. Pennings, "Optical multimode interference devices based on self-imaging - principles and applications," *Journal of Lightwave Technology*, vol. 13, no. 4, pp. 615–627, 1995, qv019 Times Cited:391 Cited References Count:69.

[31] K. P. Zetie, S. F. Adams, and R. M. Tocknell, "How does a mach-zehnder interferometer work?" *Physics Education*, vol. 35, no. 1, p. 46, 2000.

[32] H. Y. Wong, M. Sorel, A. C. Bryce, J. H. Marsh, and J. M. Arnold, "Monolithically integrated ingaas-algainas mach-zehnder interferometer optical switch using

quantum-well intermixing," *Ieee Photonics Technology Letters*, vol. 17, no. 4, pp. 783–785, 2005, 909PF Times Cited:1 Cited References Count:15.

[33] M. Vasilyev, Y. K. Su, and C. J. McKinstrie, "Introduction to the special issue on nonlinear-optical signal processing," *Ieee Journal of Selected Topics in Quantum Electronics*, vol. 14, no. 3, pp. 527–528, 2008, 311UC Times Cited:0 Cited References Count:0.

[34] M. D. Pelusi, V. G. Ta'eed, L. B. Fu, E. Magi, M. R. E. Lamont, S. Madden, D. Y. Choi, D. A. P. Bulla, B. Luther-Davies, and B. J. Eggleton, "Applications of highly-nonlinear chalcogenide glass devices tailored for high-speed all-optical signal processing," *Ieee Journal of Selected Topics in Quantum Electronics*, vol. 14, no. 3, pp. 529–539, 2008, 311UC Times Cited:0 Cited References Count:38.

[35] M. Galili, L. K. Oxenlowe, H. C. H. Mulvad, A. T. Clausen, and P. Jeppesen, "Optical wavelength conversion by cross phase modulation of data signals up to 640 gb/s," *Ieee Journal of Selected Topics in Quantum Electronics*, vol. 14, no. 3, pp. 573–579, 2008, 311UC Times Cited:0 Cited References Count:8.

[36] C. Ito and J. C. Cartledge, "Polarization independent all-optical 3r regeneration based on the kerr effect in highly nonlinear fiber and offset spectral slicing," *Ieee Journal of Selected Topics in Quantum Electronics*, vol. 14, no. 3, pp. 616–624, 2008, 311UC Times Cited:0 Cited References Count:26.

[37] A. E. Willner, B. Zhang, L. Zhang, L. S. Yan, and I. Fazal, "Optical signal processing using tunable delay elements based on slow light," *Ieee Journal of Selected Topics in Quantum Electronics*, vol. 14, no. 3, pp. 691–705, 2008, 311UC Times Cited:0 Cited References Count:90.

[38] I. Kang, C. Dorrer, L. Zhang, M. Dinu, M. Rasras, L. L. Buhl, S. Cabot, A. Bhardwaj, X. Liu, M. A. Cappuzzo, L. Gomez, A. Wong-Foy, Y. F. Chen, N. K. Dutta,

S. S. Patel, D. T. Neilson, C. R. Giles, A. Piccirilli, and J. Jaques, "Characterization of the dynamical processes in all-optical signal processing using semiconductor optical amplifiers," *Ieee Journal of Selected Topics in Quantum Electronics*, vol. 14, no. 3, pp. 758–769, 2008, 311UC Times Cited:0 Cited References Count:50.

[39] J. J. Dong, X. L. Zhang, S. N. Fu, J. Xu, P. Shum, and D. X. Huang, "Ultrafast all-optical signal processing based on single semiconductor optical amplifier and optical filtering," *Ieee Journal of Selected Topics in Quantum Electronics*, vol. 14, no. 3, pp. 770–778, 2008, 311UC Times Cited:0 Cited References Count:25.

[40] M. Scaffardi, P. Ghelfi, E. Lazzeri, L. Poti, and A. Bogoni, "Photonic processing for digital comparison and full addition based on semiconductor optical amplifiers," *Ieee Journal of Selected Topics in Quantum Electronics*, vol. 14, no. 3, pp. 826–833, 2008, 311UC Times Cited:0 Cited References Count:28.

[41] K. Hinton, G. Raskutti, P. A. Farrell, and R. S. Tucker, "Switching energy and device size limits on digital photonic signal processing technologies," *Ieee Journal of Selected Topics in Quantum Electronics*, vol. 14, no. 3, pp. 938–945, 2008, 311UC Times Cited:0 Cited References Count:52.

[42] A. J. Poustie, K. J. Blow, and R. J. Manning, "All-optical regenerative memory for long term data storage," *Optics Communications*, vol. 140, no. 4-6, pp. 184–186, 1997, xg976 Times Cited:29 Cited References Count:17.

[43] A. J. Poustie, K. J. Blow, A. E. Kelly, and R. J. Manning, "All-optical binary half-adder," *Optics Communications*, vol. 156, no. 1-3, pp. 22–26, 1998, 138FH Times Cited:29 Cited References Count:17.

[44] J. P. Sokoloff, P. R. Prucnal, I. Glesk, and M. Kane, "A terahertz optical asymmetric demultiplexer (toad)," *Ieee Photonics Technology Letters*, vol. 5, no. 7, pp. 787–790, 1993, lr940 Times Cited:242 Cited References Count:9.

[45] S. P. Dijaili, J. M. Wiesenfeld, G. Raybon, C. A. Burrus, A. Dienes, J. S. Smith, and J. R. Whinnery, "Cross-phase modulation in a semiconductor-laser amplifier determined by a dispersive technique," *Ieee Journal of Quantum Electronics*, vol. 28, no. 1, pp. 141–150, 1992, gz837 Times Cited:3 Cited References Count:24.

[46] G. Gavioli, B. C. Thomsen, V. Mikhailov, and P. Bayvel, "Cascadability properties of optical 3r regenerators based on soas," *Journal of Lightwave Technology*, vol. 25, no. 9, pp. 2766–2775, 2007, 208WN Times Cited:1 Cited References Count:19.